

1 Testing models of thorium and particle cycling in the
2 ocean using data from station GT11-22 of the U.S.

3 GEOTRACES North Atlantic Section

4 Paul Lerner*¹, Olivier Marchal¹, Phoebe J. Lam², Robert F. Anderson³, Ken
5 Buesseler¹, Matthew A. Charette¹, R. Lawrence Edwards⁴, Christopher T.
6 Hayes⁵, Kuo-Fang Huang⁶, Yanbin Lu⁴, Laura F. Robinson⁷, and Andrew Solow¹

7 ¹*Woods Hole Oceanographic Institution, Woods Hole, MA 02543, USA*

8 ²*University of California Santa Cruz, Santa Cruz, CA 95064, USA*

9 ³*Lamont-Doherty Earth Observatory, Columbia University, Palisades, NY 10964, USA*

10 ⁴*University of Minnesota, Minneapolis, MN 55455, USA*

11 ⁵*Massachusetts Institute of Technology, Cambridge, MA 02139, USA*

12 ⁶*Institute of Earth Sciences, Academia Sinica, Nangang, Taipei 11529, Taiwan*

13 ⁷*University of Bristol, Bristol BS8 1TH, UK*

14 **Abstract**

15 Thorium is a highly particle-reactive element that possesses different measurable radio-
16 isotopes in seawater, with well-constrained production rates and very distinct half-lives. As a
17 result, Th has emerged as a key tracer for the cycling of marine particles and of their chemical
18 constituents, including particulate organic carbon.

19 Here two different versions of a model of Th and particle cycling in the ocean are tested us-
20 ing an unprecedented data set from station GT11-22 of the U.S. GEOTRACES North Atlantic

*Corresponding Author. Address: Department of Marine Chemistry and Geochemistry, Woods Hole Oceanographic Institution, 266 Woods Hole Road, Clark 448 (MS#25), Woods Hole, MA (Tel:1-508-289-3278)
email address: plerner@whoi.edu

21 Section: (i) ^{228,230,234}Th activities of dissolved and particulate fractions, (ii) ²²⁸Ra activities,
22 (iii) ^{234,238}U activities estimated from salinity data and an assumed ²³⁴U/²³⁸U ratio, and (iv)
23 particle concentrations, below a depth of 125 m. The two model versions assume a single class
24 of particles but rely on different assumptions about the rate parameters for sorption reactions
25 and particle processes: a first version (V1) assumes vertically uniform parameters (a popular
26 description), whereas the second (V2) does not. Both versions are tested by fitting to the
27 GT11-22 data using generalized nonlinear least squares and by analyzing residuals normalized
28 to the data errors.

29 We find that model V2 displays a significantly better fit to the data than model V1. Thus,
30 the mere allowance of vertical variations in the rate parameters can lead to a significantly better
31 fit to the data, without the need to modify the structure or add any new processes to the model.
32 To understand how the better fit is achieved we consider two parameters, $K = k_1/(k_{-1} + \beta_{-1})$
33 and K/P , where k_1 is the adsorption rate constant, k_{-1} the desorption rate constant, β_{-1} the
34 remineralization rate constant, and P the particle concentration. We find that the rate constant
35 ratio K is large (≥ 0.2) in the upper 1000 m and decreases to a nearly uniform value of ca.
36 0.12 below 2000 m, implying that the specific rate at which Th attaches to particles relative
37 to that at which it is released from particles is higher in the upper ocean than in the deep
38 ocean. In contrast, K/P increases with depth below 500 m. The parameters K and K/P
39 display significant positive and negative monotonic relationship with P , respectively, which is
40 collectively consistent with a particle concentration effect.

41 **Keywords:** GEOTRACES;North Atlantic;Thorium;Particles;Reversible Exchange;Model;Inverse
42 Method

43 1 Introduction

44 Roughly 20-25% of carbon fixed photosynthetically by phytoplankton in near surface-waters
45 is estimated to sink as particles to depths below 100 m, with approximately 10% of this sink-
46 ing material reaching the sediments ([Bishop, 2009](#)). The sinking and subsequent remineralization
47 of particulate organic matter strongly influence the vertical concentration gradients of chemical
48 constituents in the ocean, including dissolved inorganic carbon, nutrients, and dissolved oxygen.

49 Therefore, understanding the processes that control the cycling of particles and the exchange of
50 elements between the dissolved and particulate phases is essential in order to understand the dis-
51 tribution of these constituents in the ocean.

52 The processes that impact marine particles include, e.g., (dis)aggregation, remineralization,
53 dissolution, and gravitational sinking. The radioactive isotopes of thorium have for a long time
54 been used to study these processes (for reviews see *Savoie et al. (2006)*; *Lam and Marchal (2014)*).
55 Thorium is highly particle reactive in seawater, and its isotopes are characterized by widely differ-
56 ent half-lives: $t_{1/2} = 24.101 \pm 0.025$ days for ^{234}Th (*Knight and Macklin, 1948*), $75,584 \pm 110$ yr
57 for ^{230}Th (*Cheng et al., 2013*), and 1.910 ± 0.002 yr for ^{228}Th (*Kirby et al., 2002*). Additionally,
58 the sources of these thorium isotopes in the ocean are relatively well understood. ^{234}Th , ^{230}Th , and
59 ^{228}Th are produced in situ by radioactive decay of ^{238}U , ^{234}U , and ^{228}Ra , respectively. Since ura-
60 nium seems to behave quasi-conservatively in the ocean (*Ku et al., 1977*; *Delanghe et al., 2002*),
61 the ^{234}U and ^{238}U activities are often estimated from salinity (*Chen et al., 1986*; *Owens et al.,*
62 *2011*), whereas the ^{228}Ra activity is generally measured directly (*Henderson et al., 2013*). Another
63 potential source of ^{230}Th is the dissolution of lithogenic materials, although this contribution ap-
64 pears negligible except in surface waters close to mineral dust sources (*Hayes et al., 2013*). The
65 high particle reactivity of Th combined with multiple isotopes that have a wide range of half-lives
66 makes it particularly well suited to study the variety of processes that affect particles. For example,
67 ^{230}Th has found several applications in paleo-oceanography. These include using ^{230}Th to correct
68 for sediment lateral redistribution (e.g., *François et al. (2004)*) and (in concert with ^{231}Pa) to es-
69 timate biological productivity (e.g., *Kumar et al. (1993, 1995)*) and aspects of ocean circulation
70 (e.g., *Yu et al. (1996)*).

71 The concept of scavenging, i.e., the attachment of trace metals to sinking particles and their
72 subsequent removal to the sea floor, was proposed by *Goldberg (1954)*. Subsequently, there has
73 been widespread recognition of the importance of scavenging in controlling the distribution of
74 trace metals in the ocean (*Krauskopf, 1956*; *Turekian, 1977*). *Bhat et al. (1969)* concluded from
75 ^{234}Th data obtained from the Arabian Sea, Java sea, Australian coast, Wharton Sea, and the Tasma-

76 nia coast, that the distribution of ^{234}Th is controlled by adsorption of thorium onto particles. They
77 considered an irreversible scavenging model for particulate ^{234}Th , which explained the deficit of
78 ^{234}Th relative to ^{238}U in the surface mixed layer. Their model, however, was based on the as-
79 sumption that all ^{234}Th is adsorbed onto particles. *Krishnaswami et al. (1976)*, using ^{234}Th data
80 from the Pacific GEOSECS expedition, estimated particulate ^{234}Th to be only 10-20% of the total
81 activity of ^{234}Th (dissolved and particulate). They also found ^{230}Th in the particulate phase to
82 increase approximately linearly with depth in the water column. Based on their observations, they
83 proposed a one-dimensional (vertical) scavenging model for particulate thorium, similar to that of
84 *Bhat et al. (1969)* but with an added scavenging term to account for the existence of both dissolved
85 and particulate phases.

86 *Nozaki et al. (1981)*, using data from the western North Pacific, and *Bacon and Anderson*
87 *(1982)*, using data from the Panama and Guatemala Basins, observed that the activities of ^{230}Th in
88 both dissolved and particulate forms increase generally with depth. This observation necessitated a
89 revision of the scavenging model and prompted the authors to develop a reversible exchange model
90 to account for the observed vertical distributions of dissolved and particulate ^{230}Th . The innovation
91 in this model was a term for the loss of thorium from the particles (one particle class) through
92 desorption and (or) remineralization. Since then, the reversible exchange model has become a
93 popular description of thorium isotope cycling in the oceanic water column, and many studies
94 used this model in combination with a “ventilation” term in the interpretation of ^{230}Th and ^{231}Pa
95 data (e.g., *Rutgers van der Loeff and Berger (1993)*; *Scholten et al. (1995)*; *Vogler et al. (1998)*;
96 *Moran et al. (2002)*; *Scholten et al. (2008)*; *Hayes et al. (2015a)*).

97 Nevertheless, there has been extensive modifications to the reversible exchange model with one
98 particle class. *Clegg and Whitfield (1990)* modeled thorium and particles in both small and large
99 size classes. Included in their model are terms for the aggregation of small particles and disag-
100 gregation of large particles. More recently, *Burd et al. (2000)* presented a “coupled adsorption-
101 aggregation” model, in which a particle size spectrum (particle size ranging from less than 10^{-2}
102 to $53\ \mu\text{m}$) is represented in order to interpret field observations of the particulate organic carbon

103 (POC) to ^{234}Th ratio.

104 Observational estimates of the rate constants of thorium and particle cycling in the ocean dis-
105 play large variations. They range from 0.1-1 yr^{-1} for adsorption and 1-10 yr^{-1} for desorption
106 (*Nozaki et al., 1987; Bacon and Anderson, 1982; Murnane et al., 1990; Murnane, 1994a; Murnane*
107 *et al., 1994b*), 1-100 yr^{-1} for remineralization (*Clegg et al., 1991*), 0.1-100 yr^{-1} for aggregation,
108 and 1-2500 yr^{-1} for disaggregation (*Nozaki et al., 1987; Murnane et al., 1990; Cochran et al.,*
109 *1993; Murnane et al., 1996; Cochran et al., 2000*). Likewise, estimates of the sinking speed of
110 bulk particles, including all sizes, vary widely, from 300-900 m yr^{-1} (*Krishnaswami et al., 1976,*
111 *1981; Rutgers van der Loeff and Berger, 1993; Scholten et al., 1995; Venchiarutti et al., 2008*). For
112 the average sinking speed of particles greater than 45 μm in diameter, *McDonnell and Buesseler*
113 *(2010)* found values from 10 to 150 m d^{-1} in waters near the west Antarctic Peninsula. *Turner*
114 *(2002)* reported an even larger range, from less than tens to over thousands m d^{-1} , for the sinking
115 velocity of fecal pellets. These large variations are a current impediment to any attempt to develop
116 large-scale models of particle and biogeochemical processes in the ocean.

117 In a series of studies, R. Murnane and colleagues pioneered the use of inverse methods in order
118 to estimate rate constants of particle and thorium cycling in the ocean (*Murnane et al., 1990; Mur-*
119 *nane, 1994a; Murnane et al., 1994b, 1996*). Using a generalized nonlinear least squares technique
120 (Algorithm of Total Inversion or ATI) (*Tarantola and Valette, 1982*), *Murnane (1994a)* performed
121 an inversion of Th and particle data from Station P (50° N, 145° W) in the Gulf of Alaska. He
122 compared solutions obtained from the ATI with two other regression techniques: ordinary least
123 squares and a regression procedures by *Wolberg (1967)*. He found that the solution obtained from
124 the ATI was both more realistic and consistent with prior estimates of the rate constants and with
125 data from station P than solutions obtained from the other techniques.

126 The adequacy of the ATI to infer rate constants of sorption reactions, however, was questioned
127 by *Athias et al. (2000a)* and *Athias et al. (2000b)*. These authors reported that a least squares
128 approach could not recover rate parameters of a model of Al (another relatively insoluble trace
129 metal) cycling from a simulated data set generated by the same model. They concluded that the

130 generalized least squares approach of *Tarantola and Valette (1982)* could not be applied to their
131 problem. In contrast, *Marchal and Lam (2012)* succeeded in inferring rate parameters using the
132 ATI from simulated Th and particle data. Their study suggests that field observations could be used
133 to constrain rate parameters of Th and particle processes in the ocean. Furthermore, they concluded
134 that measurements of particle and $^{228,230,234}\text{Th}$ concentrations in different size fractions, such as
135 generated during GEOTRACES, should significantly improve the precision of the rate parameters
136 inferred relative to *a priori* estimates.

137 The differences between the results of *Athias et al. (2000b)* and *Marchal and Lam (2012)* were
138 discussed by *Marchal and Lam (2012)*. These authors found that relatively large prior errors in the
139 rate parameters in combination with the constraint that the model equations be imposed exactly
140 can prevent the ATI from converging to a stable solution. Thus differences in assumptions about
141 the prior errors between these two studies may have led to different results regarding the adequacy
142 of the ATI to infer rate parameters. Besides *Murnane (1994a)*, *Murnane et al. (1994b)*, *Murnane*
143 *et al. (1996)*, and *Marchal and Lam (2012)*, other studies have successfully applied the ATI to
144 oceanographic problems (e.g., *Mercier (1986)*, *Mercier (1989)*, *Mercier et al. (1993)*, *Paillet and*
145 *Mercier (1997)*, *Marchal et al. (2007)*).

146 Here we rejuvenate the approach first applied by *Murnane (1994a)* to constrain aspects of tho-
147 rium and particle cycling from the extensive data set collected at station GT11-22 of the U.S.
148 GEOTRACES North Atlantic Section (GA03) (*Boyle et al., 2015*). Station GT11-22 was cho-
149 sen because it is an open ocean station that appears to have relatively little influence from hy-
150 drothermal vents near the Mid-Atlantic Ridge and from the Mauritanian Upwelling, both of which
151 may be regions that exhibit enhanced scavenging due to processes not encapsulated by the re-
152 versible exchange model (e.g., *Hayes et al. (2015a)*; *Lam et al. (2015)*). The GT11-22 data include
153 $^{234,230,228}\text{Th}$ activities in dissolved ($<0.8\mu\text{m}$) and particulate ($0.8\text{-}51\mu\text{m}$) phases, particle concen-
154 tration in the small ($<51\mu\text{m}$) and large ($>51\mu\text{m}$) size fractions, measurements of dissolved ^{228}Ra ,
155 and $^{234,238}\text{U}$ activities estimated from salinity data. We feel that there is as of yet insufficient data to
156 constrain a model that deals with Th and particles in both small and large particle fractions. Thus,

157 we use the data (collected at and below 125 m) in order to test two versions of a 1-D (vertical)
158 model of Th and particle cycling that considers one particle class with either vertically uniform
159 (model V1) or nonuniform (model V2) parameters. Specifically, we test whether the fit of model
160 V2 to radiochemical and particle data is significantly better than that of model V1 given the larger
161 number of degrees of freedom of a model with variable parameters. The model is similar to that
162 used by *Bacon and Anderson (1982)*, except that remineralization and desorption are treated sep-
163 arately. The model therefore neglects potentially important effects such as lateral transport. The
164 purpose of this study is to quantify the improvement of the model when the rate parameters are
165 allowed to vary with depth. This way, we provide a test to the commonly held assumption that
166 the rate parameters of Th and particle cycling are uniform along the oceanic water column (e.g.,
167 *Nozaki et al. (1987)*; *Cochran et al. (1993, 2000)*; *Hayes et al. (2015b)*).

168 This paper is organized as follows. In section 2, the GT11-22 data, the vertical interpolation,
169 the model of particle and Th cycling, and the inverse method used to combine the data and the
170 model are described. In section 3, each version of the model is fitted to the data, considering
171 errors in the data and in their vertical interpolation. A range of measures of goodness of fit are
172 calculated in order to test the consistency of each model version with the data. In section 4,
173 we discuss the robustness of the tests, their implications for oceanic Th geochemistry, and the
174 depth-dependent budgets of $^{228,230,234}\text{Th}$ at station GT11-22. An attempt to interpret particle
175 and Th isotope residuals of the fit in terms of processes missing in the model is also undertaken.
176 Conclusions follow in section 5.

177 **2 Methods**

178 **2.1 Hydrographic Setting**

179 We use the data collected aboard the R/V Knorr in November 2011 at station GT11-22 (19°26'
180 N, 29°22' W, water depth of 5014 m), approximately 700 km northwest of Cape Verde (Figure 1).
181 This station is situated in the southeast portion of the North Atlantic subtropical gyre, which is
182 under the influence of the southwestward flow of the Northern Equatorial Current (NEC, *Stramma*
183 *et al. (2005)*). The potential temperature (θ) and salinity (S) measured by the CTD at station

184 GT11-22 (Figure 2) reveal the presence of distinct water masses, defined here according to *Jenkins*
185 *et al.* (2015). Between 80 and 554 m, the North Atlantic Central Water (NACW) and Atlantic
186 Equatorial Water (AEW) are carried to station GT11-22 by the NEC (*Schmitz and McCartney,*
187 *1993; Stramma et al., 2005*). In this depth range, NACW represents between 71% and 98% of
188 the total mass according to the water property analysis of *Jenkins et al.* (2015). The "kink" in the
189 $\theta - S$ diagram at about 230 m ($\theta \simeq 15^\circ\text{C}$, $S \simeq 36$) may be due to the replacement of NACW by
190 AEW, decreasing the relative abundance of NACW from about 88% to 71% at that depth. *Jenkins*
191 *et al.* (2015) estimated that east of 22° W, nearly all water down to 500 m is AEW. While station
192 GT11-22 is near 30° W, it is well within the influence of AEW, which contributes about 30% of
193 the thermocline waters at this site. Between 609 and 904 m, the Mediterranean Outflow Water
194 (MOW), the Antarctic Intermediate Water (AAIW), and the Irminger Sea Water (ISW) become
195 dominant. The transition between the thermocline (NACW and AEW) and intermediate waters is
196 not conspicuous in the $\theta - S$ diagram, largely because the effect of the relatively salty and warm
197 MOW tends to be offset by the fresher and colder AAIW. Between 940 and 1200 m, the Upper
198 Circumpolar Deepwater (UCDW) and the Upper Labrador Sea Water (ULSW) become important.
199 Salinity increases with depth because the relatively fresh AAIW, the dominant component at shall-
200 lower depths, decreases to about 0% at 1200 m (*Jenkins et al., 2015*). Nearly all water is comprised
201 of ULSW and UCDW between 1200 and 1900 m. The deep water masses below 2000 m include
202 the Classical Labrador Sea Water (CLSW) and two components of North Atlantic Deep Water:
203 the Denmark Straits Overflow Water (DSOW) and the Iceland-Scotland Overflow Water (ISOW).
204 Finally, the lower 2000 m of the water column at station GT11-22 is bathed by Antarctic Bottom
205 Water (AABW). This water flows northward in the western South Atlantic, crosses the equator, and
206 penetrates into the eastern basins of the North Atlantic through the Vema Fracture Zone cutting the
207 Mid-Atlantic Ridge near 11°N (*Schmitz and McCartney, 1993*).

208 **2.2 Data**

209 The following systems were used to collect the samples. The particulate, dissolved ^{228}Th , and
210 dissolved ^{228}Ra data used in this paper were obtained from samples collected by large volume

211 in-situ filtration. The dissolved ^{230}Th and ^{234}Th measurements were gathered using 30-L Niskin
212 bottles. For the collection of ^{234}Th samples below 1000 m, these bottles were attached individually
213 to the pump wire at the depths of the in-situ pumps. For the collection of dissolved ^{230}Th samples
214 at all depths and ^{234}Th samples above 1000 m, these bottles were mounted on the ODF/SIO rosette
215 on a separate cast. All Niskin and in-situ pump casts were operated over the course of the 26-hour
216 occupation of the station. These data can be found in the GEOTRACES Intermediate Data Product
217 ([Mawji and et al., 2015](#)).

218 **2.2.1 Particle concentration**

219 In this paper, P denotes particle concentration in units of $\mu\text{g m}^{-3}$. Size fractionated particles
220 were collected by large volume in-situ filtration using a modified dual-flow WTS-LV McLane
221 research pump equipped with 142-mm “mini-MULVFS” filter holders ([Bishop et al., 2012](#)). One
222 filter holder was loaded with a 51- μm Sefar polyester mesh prefilter followed by paired Whatman
223 QMA quartz fiber filters (1 μm nominal pore size). The other filter holder was also loaded with
224 another 51- μm polyester prefilter, but followed by paired 0.8- μm Pall Supor800 polyethersulfone
225 filters. The particles retained on the quartz filters were used to analyze total particulate carbon
226 and particulate inorganic carbon, while those retained on the polyethersulfone filters were used to
227 analyze biogenic silica and particulate trace metals ([Lam et al., 2015](#); [Ohnemus and Lam, 2015](#)).
228 Particle concentrations were determined from the sum of the chemical dry weight of the major
229 particles phases: particulate organic matter, particulate inorganic carbon, biogenic silica, lithogenic
230 material estimated from total particulate aluminum, and Fe and Mn oxyhydroxides ([Lam et al.,](#)
231 [2015](#)).

232 **2.2.2 ^{234}Th and ^{238}U**

233 In this paper, the subscript d (p) designates the Th isotope activity in dissolved (particulate)
234 form in units of dpm m^{-3} , e.g., $^{234}\text{Th}_d$ denotes the activity of ^{234}Th in the $<1\mu\text{m}$ size fraction
235 (QMA) and $^{234}\text{Th}_p$ denotes the activity of ^{234}Th in the $>1\mu\text{m}$ size fraction (similar designations are

236 adopted for ^{230}Th and ^{228}Th). $^{234}\text{Th}_{tot}$ designates total (dissolved + particulate) ^{234}Th . Particulate
237 ^{234}Th activities on the 1-51 μm (QMA filter) and $>51\mu\text{m}$ size fractions from in-situ filtration were
238 determined by beta counting (*Maiti et al., 2012; Owens et al., 2015*). Small volume (4 L) samples
239 for $^{234}\text{Th}_{tot}$ were obtained using an ODF/SIO Rosette above 1000 m or Niskin bottles hung above
240 the McLane pump below 1000 m, and were also analyzed using beta counting (*Owens et al., 2015*).
241 ^{238}U is estimated from salinity using the empirical equation derived by *Owens et al. (2011)*,

$$^{238}\text{U} = 0.0786(\pm 0.00446)S - 0.315(\pm 0.158), \quad (1)$$

242 where ^{238}U is in dpm m^{-3} and S is on the Practical Salinity Scale of 1978. The uncertainties
243 of ^{238}U are estimated by the root mean square error of the linear regression of ^{238}U with salinity
244 (*Owens et al., 2011*).

245 **2.2.3 ^{230}Th and ^{234}U**

246 Subsamples of polyethersulfone filters were acid digested and co-precipitated with Fe after com-
247 plete dissolution. Particulate ^{230}Th in the small (0.8-51 μm) size fraction was determined on the
248 subsamples by inductively coupled plasma mass spectrometry (ICP-MS) (*Hayes et al., 2015a*).
249 Subsamples for dissolved ^{230}Th were obtained using Niskin bottles attached to an ODF/SIO Rosette,
250 and gravity filtered through Pall Acropak 500 filters containing a 0.8- μm prefilter followed by a
251 0.45- μm filter. Dissolved ^{230}Th was also measured by ICP-MS (*Anderson et al., 2012; Shen et al.,*
252 *2012; Hayes et al., 2015b*). Finally, ^{234}U is estimated from ^{238}U by assuming a $^{234}\text{U}/^{238}\text{U}$ ratio of
253 1.147 (*Andersen et al., 2010*). The uncertainties in ^{234}U are obtained by multiplying the uncertain-
254 ties in ^{238}U by 1.147, i.e., the effect of the uncertainty in $^{234}\text{U}/^{238}\text{U}$ is neglected.

255 **2.2.4 ^{228}Th and ^{228}Ra**

256 Particulate ^{228}Th in the small (1-51 μm) size fraction sampled by in-situ filtration was mea-
257 sured by alpha delayed coincidence counting of QMA filters (*Maiti et al., 2015*). Dissolved ^{228}Ra
258 and ^{228}Th were collected simultaneously with particles by sorption on MnO_2 impregnated acrylic

259 cartridges located downstream of the two filter holders. They were analyzed by alpha delayed
 260 coincidence (^{228}Th) and gamma counting (^{228}Ra) (*Henderson et al., 2013; Charette et al., 2015*).

261 **2.3 Bulk Particulate $^{228,230,234}\text{Th}$**

262 Observational estimates of $^{228,230,234}\text{Th}$ activities for the whole particulate fraction (sizes
 263 $>1\mu\text{m}$) are obtained as follows. $^{228,230,234}\text{Th}$ activities have been measured on the small parti-
 264 cles ($1-51\mu\text{m}$). ^{234}Th data for large particles are available only in the top 900 m, and $^{228,230}\text{Th}$
 265 data for large particles are currently not available. In order to obtain bulk particle data for each
 266 Th isotope, the ratio of large ($^{234}\text{Th}_{p,l}$) to small particulate ^{234}Th ($^{234}\text{Th}_{p,s}$) is calculated from the
 267 $^{234}\text{Th}_{p,l}$ and $^{234}\text{Th}_{p,s}$ data available for the upper 900 m and below the euphotic zone (below 125 m,
 268 $n = 5$). This ratio (mean of 0.19 with a standard deviation of 0.01) is then applied to derive $^{234}\text{Th}_{p,l}$
 269 below 900 m and $^{228,230}\text{Th}_{p,l}$ at all depths, from the measured activities on the small size fraction.
 270 The measured or calculated $^{228,230,234}\text{Th}_{p,l}$ is added to the measured $^{228,230,234}\text{Th}_{p,s}$ to obtain total
 271 particulate Th for each isotope (e.g., $^{228}\text{Th}_p = ^{228}\text{Th}_{p,s} + ^{228}\text{Th}_{p,l}$). Additionally, dissolved ^{234}Th
 272 (not measured at station GT11-22) is obtained by subtracting $^{234}\text{Th}_p$ from total ^{234}Th and its error
 273 is derived by error propagation neglecting error covariance (*Bevington and Robinson, 1992*).

274 **2.4 Vertical Interpolation**

275 The depths at which P , $^{228,230,234}\text{Th}_{d,p}$, $^{234,238}\text{U}$, and ^{228}Ra data are available do not generally
 276 coincide exactly (Appendix A). In order to facilitate the data analysis, the measured (or calculated)
 277 values of P , $^{228,230,234}\text{Th}_{d,p}$, $^{234,238}\text{U}$, and ^{228}Ra are interpolated onto an irregular grid in which each
 278 grid point is at a depth where at least one measurement is available. The shallowest and deepest
 279 points of the grid are at 125 and 4243 meters, respectively. Such a grid is chosen in order (i) to
 280 exclude surface waters where processes of particle production, which are outside the scope of this
 281 study, occur, and (ii) to avoid the need for data extrapolation. We use an objective interpolation
 282 technique (e.g., *Wunsch (2006)*): an estimate of property x at depth level i , \hat{x}_i , is taken as a linear
 283 combination of the measurements of that property at all depths, x_k ($k = 1, 2, \dots, n$),

$$\hat{x}_i = \sum_{k=1}^n w_{ik} x_k, \quad (2)$$

284 where the weighting factors w_{ik} are determined such that the \hat{x}_i errors have minimum variance.

285 The interpolation requires the prescription of two matrices: a covariance matrix for the mea-
286 surement errors and a matrix describing the vertical covariance of the property being interpolated.
287 The first matrix is taken as diagonal, where the diagonal elements are the squared errors in the
288 measurements. The (i, j) element of the second matrix is taken as $\sigma_M^2 e^{-|z_i - z_j|/l_z}$, where σ_M^2 is
289 the variance of the property and l_z is a length scale characterizing its vertical covariance. The
290 quantities σ_M^2 and l_z have the following interpretation. When the interpolation depth is far from
291 the measurement depth, the error in the interpolated value approaches the square root of the field
292 property variance σ_M^2 . So, σ_M^2 is the maximum tolerable variance in the gridded (interpolated)
293 data. On the other hand, l_z is an e-folding length scale: if the distance between two depths in the
294 water column increases by l_z , the property covariance between both depths is reduced by a factor
295 of $1/e$.

296 Figure 3 shows three interpolation scenarios obtained with $\sigma_M^2 = 0.25\sigma_d^2$, $0.5\sigma_d^2$, or σ_d^2 ($l_z =$
297 1000 m in all cases), where σ_d^2 is the variance in a particular data set (e.g., the variance in the
298 $^{230}\text{Th}_d$ data). Besides differences in uncertainty in the interpolated values (Figure 3a-c), the agree-
299 ment between the interpolated and measured values at the measurement depths deteriorates as
300 σ_M^2 decreases (Figure 3d-f). This is because σ_M^2 influences the weight of each measurement in
301 the interpolated values: the larger the variance, the better the ability of the interpolated values to
302 approach the measured values. Thus, increasing σ_M^2 improves the agreement of the interpolated
303 values with the measured values, although each scenario tends to overfit the data according to
304 the normal distribution (Figure 3d-f). Decreasing σ_M^2 to less than $0.25\sigma_d^2$ (not shown) results in
305 interpolated data errors that are smaller than the uncertainties in the measurements, which is not
306 desirable. Therefore, we retain $\sigma_M^2 \geq 0.25\sigma_d^2$ in this study.

307 Figure 4 shows three other interpolation scenarios with the same values of $\sigma_M^2 = 0.5\sigma_d^2$ but
308 with different values of $l_z = 500$ m, 1000 m, or 2000 m. These different length scales capture
309 scenarios in which there is varying vertical correlation between property values at different depths.
310 As l_z increases, the error of the interpolated values decreases (Figure 4a-c). For the three values of

311 l_z , the interpolated values are consistent with the measured values, although each scenario displays
 312 an overfit to the measurements according to the normal distribution (Figure 4d-f). In this paper, we
 313 choose $\sigma_d^2 = 0.5\sigma_M^2$ and $l_z = 1000$ m as our reference interpolation. Different sets of interpolated
 314 values of P , $^{228,230,234}\text{Th}_{d,p}$, $^{234,238}\text{U}$, and ^{228}Ra are considered in section 3.

315 Figure 5 shows the measured and interpolated values of the various radiochemical activities at
 316 station GT11-22 ($\sigma_d^2 = 0.5\sigma_M^2$, $l_z = 1000$ m). The measured and interpolated values of $^{230}\text{Th}_d$ and
 317 $^{230}\text{Th}_p$ show increases with depth. However, $^{230}\text{Th}_p$ is in general relatively uniform below 2000 m,
 318 as is dissolved ^{230}Th below 3500 m. Particulate ^{234}Th decreases generally with depth to 2000 m,
 319 and shows reduced variations below. Total ^{234}Th varies between 2100 and 2700 dpm m^{-3} , with
 320 no clear systematic changes with depth. Finally, the profiles of dissolved and particulate ^{228}Th
 321 generally resemble that of the parent isotope, ^{228}Ra , with maxima in surface and bottom waters
 322 and minima at mid-depth.

323 2.5 Model of Thorium and Particle Cycling

324 We consider a model of thorium and particle cycling that includes a balance equation for each
 325 thorium isotope in each phase (dissolved and particulate), and a balance equation for bulk (large +
 326 small) particles (Figure 6). The model accounts for adsorption of thorium to particles, desorption
 327 of Th from particles, radioactive production and decay, remineralization of particles, and sinking
 328 of particles. The balance equations are (*Nozaki et al., 1981; Bacon and Anderson, 1982*)

$$0 = \lambda A_\pi + (k_{-1} + \beta_{-1})A_p - (k_1 + \lambda)A_d, \quad (3a)$$

$$w \frac{\partial A_p}{\partial z} = k_1 A_d - (\beta_{-1} + k_{-1} + \lambda)A_p, \quad (3b)$$

$$w \frac{\partial P}{\partial z} = -\beta_{-1}P. \quad (3c)$$

329 Here A_d (A_p) is the thorium isotope activity in dissolved (particulate) form (dpm m^{-3}), A_π is
 330 the activity of the radioactive parent (dpm m^{-3}), P is the particle concentration ($\mu\text{g m}^{-3}$), and
 331 λ is the radioactive decay constant (yr^{-1}). The rate parameters of the model are the adsorption
 332 rate constant (k_1 , yr^{-1}), the desorption rate constant (k_{-1} , yr^{-1}), the remineralization rate constant

333 (β_{-1} , yr^{-1}), and the particle sinking speed (w , m yr^{-1}). The presence of the vertical derivative in
334 equations (3b-3c) requires the prescription of boundary conditions, which we take as the values of
335 A_p and P at $z = 125$ m. Two model versions are considered: version V1 assumes uniform rate
336 parameters, whereas version V2 allows these parameters to vary with depth.

337 Note the various assumptions in the Th and particle cycling model (besides the assumption of
338 uniform rate parameters in model V1). Equations (3a-3c) rely on steady state and omit the effects
339 of water transport by advection and diffusion. They assume that sorption and remineralization
340 processes obey first-order kinetics. The potential sources of dissolved and particulate Th from
341 lithogenic contributions are taken as negligible. This assumption should be valid for $^{228,234}\text{Th}$, at
342 least in the surface ocean where the activities of both isotopes are generally large. Following the
343 procedures documented in *Roy-Barman et al. (2002)* and *Hayes et al. (2013)*, we calculate the
344 percent contribution of lithogenic ^{230}Th to the measured $^{230}\text{Th}_{d,p}$ using dissolved and particulate
345 ^{232}Th data at station GT11-22 (*Anderson et al., 2012; Hayes et al., 2015a*). We find that lithogenic
346 $^{230}\text{Th}_d$ always accounts for less than 10% of total $^{230}\text{Th}_d$. Lithogenic $^{230}\text{Th}_p$ accounts for up to 30%
347 of total $^{230}\text{Th}_p$ in the upper 500 m, but less than 10% below 500 m. Unless stipulated otherwise, we
348 do not correct ^{230}Th for a lithogenic contribution (the sensitivity of our results to such a correction
349 is examined in section 4.1.2).

350 **2.6 Inverse Method**

351 The ATI (*Tarantola and Valette, 1982*) is used to combine the Th and particle cycling model (sec-
352 tion 2.5) with the radiochemical and particle measurements at station GT11-22 (sections 2.2-2.4):
353 model V1 and V2 are fitted to the data, and their respective ability to explain the data is assessed
354 from the residuals of the fit. The rate parameters ($k_1, k_{-1}, \beta_{-1}, w$) as well as the radiochemical ac-
355 tivities and particle concentrations are adjusted so as to obtain the best fit. Thus the particle and
356 radiochemical data are not fixed to their measured (interpolated) values but are allowed to change
357 in the inversion within a range consistent with their estimated uncertainties. This approach allows
358 us to give due consideration to the errors in the radiochemical and particle data when testing model
359 V1 and V2 (see discussion in *Lam and Marchal (2014)*).

360 A brief description of the ATI follows. Let \mathbf{x} be a vector describing the state of the Th and
 361 particle cycles according to the model. The elements of \mathbf{x} are the Th isotope activities in the dis-
 362 solved and particulate phases, the particle concentrations, the parent activities (^{234}U , ^{238}U , ^{228}Ra),
 363 as well as the rate parameters ($k_1, k_{-1}, \beta_{-1}, w$). In model V1, \mathbf{x} includes these variables at all depths
 364 of the grid at station GT11-22 (section 2.4), except for the uniform rate parameters. In model V2,
 365 \mathbf{x} includes these variables at all depths of the grid. The objective is to find a vector \mathbf{x} that fits sta-
 366 tion GT11-22 (interpolated) data given their error statistics, while satisfying the model equations
 367 (3a-3c) perfectly. This vector is found at a stationary point of the objective function:

$$J = (\mathbf{x} - \mathbf{x}_0)^T \mathbf{C}_0^{-1} (\mathbf{x} - \mathbf{x}_0) + \mathbf{x}^T \mathbf{S}^{-1} \mathbf{x} - 2\mathbf{u}^T \mathbf{f}(\mathbf{x}). \quad (4)$$

368 Here, \mathbf{x}_0 is a vector including prior estimates of the elements in \mathbf{x} (in our study, the interpolated
 369 data and prior estimates of rate parameters), \mathbf{C}_0 is the error covariance matrix for the prior esti-
 370 mates (the diagonal elements of \mathbf{C}_0 are the squared errors in the estimates and the off-diagonal
 371 elements of \mathbf{C}_0 are the covariances between the errors), \mathbf{S}^{-1} is another square matrix, \mathbf{u} is a vector
 372 of Lagrange multipliers, and $\mathbf{f}(\mathbf{x}) = \mathbf{0}$ is a vector including the difference equations derived from
 373 (3a-3c), with $w\partial A_p/\partial z$ and $w\partial P/\partial z$ discretized with a first-order backward scheme.

374 The three terms of the objective function (4) have the following interpretations. The first term
 375 represents the deviation of the state vector from its prior estimate, where \mathbf{C}_0 plays the role of a
 376 weighting factor: the elements of \mathbf{x}_0 with small (large) uncertainties contribute strongly (modestly)
 377 to the objective function. The second term prescribes a certain amount of smoothing on the vertical
 378 variation of some elements of \mathbf{x} (see below). Finally, the third term is the hard constraint imposed
 379 in the search for a stationary point of J . Thus, we search for a minimum of the sum of the first
 380 two terms, subject to the hard constraint $\mathbf{f}(\mathbf{x}) = \mathbf{0}$. The prior estimates of the rate parameters and
 381 their errors are based on observational estimates published in the literature (Table 1; section 1).

382 The motive for including the smoothing term $\mathbf{x}^T \mathbf{S}^{-1} \mathbf{x}$ in J is twofold. First, since some of the
 383 prior estimates contain large errors, it is possible that some elements of the solution are negative,

Table 1: Prior estimates of rate parameters of Th and particle cycling assumed in this study

parameter	prior estimate	prior estimate error
k_1 (y^{-1})	0.5	5
k_{-1} (y^{-1})	2	5
β_{-1} (y^{-1})	1	10
w ($m y^{-1}$)	700	400

384 which is nonsensical in our study. Preliminary inversions have shown that negative values tend to
 385 not occur when some smoothing is imposed to the solution. Second, the imposition of smoothing
 386 tends to prevent large variations of solution elements on small vertical scales, which do not appear
 387 geochemically plausible. Here \mathbf{S}^{-1} only acts on the rate parameters $(k_1, k_{-1}, \beta_{-1}, w)$. The non-
 388 vanishing elements of $\mathbf{x}^T \mathbf{S}^{-1} \mathbf{x}$ have the generic form

$$\gamma (x(z_2) - x(z_1))^2, \quad (5)$$

389 where x represents k_1 , k_{-1} , β_{-1} , or w , z_1 and z_2 are two different depths, and the parameter γ
 390 trades smoothness of the solution against its proximity to the data. In our study, γ is set equal to 1,
 391 unless stipulated otherwise. The effect of γ on our results is examined in section 4.1.

392 The dimensions of the vector \mathbf{x} and $\mathbf{f}(\mathbf{x})$ are as follows. The number of grid points is 41, but
 393 since the shallowest grid point is where the boundary conditions of the model are imposed, the
 394 $^{234,238}\text{U}$, ^{228}Ra , and $^{228,230,234}\text{Th}_d$ activities are defined at 40 depths, while the $^{228,230,234}\text{Th}_p$ activ-
 395 ities and P concentrations are defined at all depths. Furthermore, there are 40 equations for each
 396 Th isotope in each phase (dissolved and particulate), as well as 40 equations for the particle con-
 397 centration. As a result, there are $M = 280$ equations (elements of $\mathbf{f}(\mathbf{x})$) and $N = 408$ unknowns
 398 (elements of \mathbf{x}) for model V1, and there are $M = 280$ equations and $N = 564$ unknowns for
 399 model V2. In both cases, the fit of the model equations to the data is an underdetermined problem.

The ATI can be derived as follows. The model equations $\mathbf{f}(\mathbf{x})$ are linearized, i.e., $\mathbf{f}(\mathbf{x}_{k+1}) = \mathbf{f}(\mathbf{x}_k) + \mathbf{F}_k(\mathbf{x}_{k+1} - \mathbf{x}_k)$, where \mathbf{x}_{k+1} and \mathbf{x}_k denote two different values of \mathbf{x} , and \mathbf{F}_k is a matrix whose elements are the partial derivatives of the model equations with respect to the elements of \mathbf{x} , i.e., the element in the i th row and j th column of \mathbf{F}_k is $\partial f_i / \partial x_j$. Setting $\partial J / \partial \mathbf{x} = \mathbf{0}$ and $\partial J / \partial \mathbf{u} = \mathbf{0}$ then leads to a system of linear algebraic equations from which an iterative procedure

to find \boldsymbol{x} can be derived. The solution for \boldsymbol{x} at the $(k+1)$ th iteration and its error covariance matrix are given by, respectively:

$$\hat{\boldsymbol{x}}_{k+1} = \boldsymbol{P}_k \boldsymbol{x}_0 + \boldsymbol{C}_{os} \boldsymbol{F}_k^T (\boldsymbol{F}_k \boldsymbol{C}_{os} \boldsymbol{F}_k^T)^{-1} \boldsymbol{b}_k, \quad (6)$$

$$\boldsymbol{C}_{k+1} = \boldsymbol{P}_k \boldsymbol{C}_0 \boldsymbol{P}_k^T, \quad (7)$$

where

$$\boldsymbol{P}_k = \boldsymbol{C}_{os} \boldsymbol{C}_0^{-1} - \boldsymbol{C}_{os} \boldsymbol{F}_k^T (\boldsymbol{F}_k \boldsymbol{C}_{os} \boldsymbol{F}_k^T)^{-1} \boldsymbol{F}_k \boldsymbol{C}_{os} \boldsymbol{C}_0^{-1}, \quad (8)$$

$$\boldsymbol{b}_k = \boldsymbol{F}_k \hat{\boldsymbol{x}}_k - \boldsymbol{f}(\boldsymbol{x}_k), \quad (9)$$

$$\boldsymbol{C}_{os} = (\boldsymbol{C}_0^{-1} + \boldsymbol{S}^{-1})^{-1}. \quad (10)$$

400 The iterative procedure is initiated at $\hat{\boldsymbol{x}}_{k=0} = \boldsymbol{x}_0$ and terminated when the relative difference
 401 between two subsequent values of each element of $\hat{\boldsymbol{x}}$ is less than 1% in absolute magnitude. The
 402 estimate of \boldsymbol{x} obtained at this stage is noted $\hat{\boldsymbol{x}}$ and referred to as the solution of the fit of model V1
 403 or V2 to GT11-22 data.

404 To ensure that the Th and particle equations in $\boldsymbol{f}(\boldsymbol{x}) = \mathbf{0}$ have a commensurate effect in
 405 the inversion, independent of the choice of units, the elements of \boldsymbol{x} are normalized by their prior
 406 values in \boldsymbol{x}_0 prior to the operation of the ATI. Accordingly, all elements of \boldsymbol{x}_0 are set equal to 1
 407 and all elements of \boldsymbol{C}_0 are scaled by the squared errors in the prior estimates. Additionally, each
 408 model equation is normalized by the root of the sum of the squared terms in that equation. This
 409 normalization scheme forces the leading terms in each equation to be roughly on the same order
 410 of magnitude, so that the effect of each equation should be similar in the inversion.

411 **3 Results**

412 In this section, the two versions of the Th and particle cycling model (V1 and V2; section 2.4) are
 413 fitted to the station GT11-22 data (sections 2.2-2.4) using the ATI (section 2.5). The fitted values
 414 of $^{234,238}\text{U}$, ^{228}Ra , $^{228,230,234}\text{Th}_{d,p}$ and particle concentration are plotted in Figure 7 for model V1
 415 and Figure 8 for model V2. For both versions, convergence to a stable solution is reached after 14
 416 iterations. In order to check whether the model equations are satisfied by the solution $\hat{\boldsymbol{x}}$ given the

417 inevitable numerical errors involved in the matrix operations (6-10), the residual of each equation,
 418 $f_i(\hat{\mathbf{x}}) = \epsilon_i$, is calculated and compared with the maximum term in the corresponding equation. For
 419 each fit (V1 or V2), we find that the residual ϵ_i amounts to less than 10^{-3} (in absolute magnitude)
 420 of the maximum term for each equation, indicating that the model equations are satisfied to at least
 421 the 3rd order.

422 3.1 Goodness of fit

423 Two measures of goodness of fit of model V1 and V2 to GT11-22 data are considered. A
 424 first measure is the fraction (ϕ below) of the normalized residuals that are less than 2 in absolute
 425 magnitude, where a normalized residual is defined as

$$r_i = \frac{\hat{x}_i - x_{d,i}}{\sigma_{d,i}}, i = 1, 2, \dots, n. \quad (11)$$

426 Here \hat{x}_i is the estimated value of the i th variable ($^{228,230,234}\text{Th}_{d,p}$, $^{234,238}\text{U}$, ^{228}Ra , and P) in the
 427 vector $\hat{\mathbf{x}}$ that is obtained from the fit of model V1 or V2 to GT11-22 data, $x_{d,i}$ is the measured (not
 428 interpolated) value of this variable, $\sigma_{d,i}$ is the error in this measured value, and n is the number of
 429 measured values. The interpretation of ϕ is straightforward. For example, a value of 0.95 for ϕ
 430 would mean that the model version being considered can be brought into consistency with 95% of
 431 the GT11-22 data given their errors.

432 The second measure of goodness of fit is the arithmetic average of the difference between the
 433 estimated and measured values, normalized by the measurement error:

$$B = \frac{1}{n} \sum_{i=1}^n \frac{\hat{x}_i - x_{d,i}}{\sigma_{d,i}}. \quad (12)$$

434 In general, a relatively large absolute value of B would indicate a relatively large bias of the
 435 corresponding model version in describing the GT11-22 data. The quantities ϕ and B are com-
 436plementary measures of goodness of fit: ϕ describes the overall ability of model V1 or V2 to fit
 437 GT11-22 data with no regard for possible under- or over-estimation, whereas B should be indica-
 438 tive of systematic errors in the model versions.

439 We find that the version of the Th and particle cycling model that assumes vertically uniform
 440 rate parameters (model V1) can fit 52%-55% of the GT11-22 data ($0.52 \leq \phi \leq 0.55$), where
 441 the range reflects varying assumptions for vertical interpolation (Table 2). In contrast, the model
 442 version that permits vertical variations in $k_1, k_{-1}, \beta_{-1}, w$ (model V2) can explain 73%-78% of the
 443 GT11-22 data, where the range reflects again varying assumptions about σ_M^2 and l_z .

Table 2: Measures of goodness of fit of model V1 and V2 to station GT11-22 data^a.

	$\sigma_M^2 = 0.5\sigma_d^2$	$\sigma_M^2 = \sigma_d^2$	$\sigma_M^2 = 0.25\sigma_d^2$	$l_z = 2000$ m	$l_z = 500$ m
ϕ for V1	0.54	0.55	0.52	0.52	0.55
ϕ for V2	0.74	0.76	0.73	0.73	0.78
B for V1	-1.91	-1.86	-2.00	-1.96	-1.89
B for V2	-0.45	-0.40	-0.53	-0.49	-0.41

a. For each listed $\sigma_M^2, l_z=1000$ m. For each listed $l_z, \sigma_M^2 = 0.5\sigma_d^2$

444 The model version that allows vertical variations in the rate parameters produces a better fit to
 445 the observations than the version that does not. This result holds as the interpolation parameters are
 446 varied within plausible ranges, e.g., $0.25\sigma_d^2 \leq \sigma_M^2 \leq \sigma_d^2$ and $500 \text{ m} \leq l_z \leq 2000 \text{ m}$. Moreover, the
 447 bias of model V2 ($-0.53 \leq B \leq -0.40$) is always less than for model V1 ($-2.00 \leq B \leq -1.86$),
 448 indicating that allowance of vertical variations of k_1, k_{-1}, β_{-1} , and w reduces the systematic errors
 449 of the Th and particle cycling model (Table 2).

450 3.2 Bootstrap Test

451 To compare models V1 and V2, we perform a parametric bootstrap test ([Efron and Tibshirani,](#)
 452 [1993](#)) of the null hypothesis H_0 that V1 is correct against the alternative hypothesis H_1 that V2 is
 453 correct. Let $x_{d,i}$ be a measured value with standard deviation $\sigma_{d,i}$ and let $\hat{x}_{1,i}$ be the corresponding
 454 fitted value for V1. The goodness of fit of V1 to all n measurements can be determined by:

$$J_d(V1) = \sum_{i=1}^n \left(\frac{\ln(x_{d,i}) - \ln(\hat{x}_{1,i})}{\sigma_{\ln(x_{d,i})}} \right)^2, \quad (13)$$

455 where

$$\sigma_{\ln(x_{d,i})} = \sqrt{\ln \left(1 + \frac{\sigma_{d,i}^2}{x_{d,i}^2} \right)}. \quad (14)$$

456 is an estimate of the standard deviation of $\ln(x_{d,i})$ (Vanmarcke, 1983). The test statistic used in the
457 parametric bootstrap procedure is:

$$T = J_d(V1) - J_d(V2), \quad (15)$$

458 where $J_d(V2)$ is the analogue of (13) for V2. The quantity T measures the improvement in fit by
459 relaxing the constraint of parameter uniformity in model V1.

460 The parametric bootstrap test proceeds by (i) simulating a set of measurements from the fitted
461 model V1,

$$x_{d,i}^* = e^{\ln(\hat{x}_{1,i}) + \epsilon_i}, \quad i = 1, 2, \dots, n \quad (16)$$

462 where ϵ_i is normally distributed with mean 0 and standard deviation $\sigma_{\ln(x_{d,i})}$, (ii) re-fitting V1 and
463 V2 to the simulated observations, and (iii) forming the corresponding value of the test statistic T .
464 The procedure is repeated a total of 200 times and the observed significance level (or p value) is
465 approximated by the proportion of occurrences the simulated value of T exceeds the value for the
466 original data ($T = 7170$).

467 A histogram of the values of T generated by this bootstrap procedure is shown in Figure 9
468 along with the observed value. In this case, none of these values exceeds the observed value, so
469 model V1 can be rejected in favor of model V2.

470 3.3 Consistency with Prior Estimates

471 A question of geochemical interest is whether the rate parameters $(k_1, k_{-1}, \beta_{-1}, w)$ that are ob-
472 tained from the fit of model V2 to GT11-22 data vary within plausible ranges. To address this
473 question, we compare the vertical variations of $(k_1, k_{-1}, \beta_{-1}, w)$ obtained from the fit with the prior
474 estimates of these parameters (Figure 10). The posterior estimates of k_1 , k_{-1} , β_{-1} , and w are all
475 within two standard deviations of the prior estimates, indicating that the rate parameters inferred
476 from the fit of model V2 to GT11-22 data are consistent with prior knowledge. The most signifi-
477 cant differences between the prior and posterior values occur for the particle sinking speed (Figure

478 10d), a result elaborated upon below (section 4.2). Note also the dramatic reduction in the prior un-
479 certainties in $(k_1, k_{-1}, \beta_{-1}, w)$ that results from the combination of model V2 with station GT11-22
480 data (Figure 10).

481 **4 Discussion**

482 Our results indicate that a model with depth-dependent rate parameters provides a significantly
483 better description of particle concentration and thorium activity data at station GT11-22 than a
484 model with uniform rate parameters. While non-negative rate parameters are obtained for both
485 model V1 and V2, there is a disconcerting feature in both solutions: ^{228}Ra values inferred by
486 inversion near 500 m are negative, which is nonsensical (Figure 7 and 8). These values differ
487 from 0 dpm m^{-3} by more than one standard deviation. While these negative values are evidence
488 that the model is not consistent with the data, we think that by themselves they do not warrant
489 definitive rejection of the model. In testing model V1 and V2, any solution elements that deviate
490 significantly from the data, not only negative values, should be interpreted as a failure to explain
491 the entire data set. Generally, one does not definitively reject a model because a few observations
492 cannot be replicated. Indeed, the model may still replicate most of the observations, and thus
493 provide a useful (albeit clearly not exact) description. The negative ^{228}Ra values are a reflection of
494 inconsistencies between the data and the model, which should be understood before a decision is
495 made about the plausibility of the model.

496 The importance of using a data set consisting of multiple thorium isotope and particle mea-
497 surements is highlighted in Figure 11. In this figure, we consider the more usual situation where
498 data for only one Th isotope (here ^{230}Th) are available. In order to test model V1, the $^{230}\text{Th}_d$ and
499 $^{230}\text{Th}_p$ data would be individually regressed linearly versus depth (*Nozaki and Nakanishi, 1985*;
500 *Edmonds et al., 1998*; *Okubo et al., 2012*) (here a weighted least squares regression is used). The
501 $^{230}\text{Th}_p$ values estimated by regression are comparable with those estimated from the entire data
502 set (compare solid line with grey circles in Figure 11b). In contrast, the $^{230}\text{Th}_d$ values from the
503 regression are systematically larger than those inferred from the entire data set and much closer to
504 the measurements (Figure 11a). With only ^{230}Th data available, one might perhaps conclude that

505 model V1 provides an adequate description of the data, which contrasts with the conclusion drawn
506 from the multiple thorium isotope and particle concentration data set. This result illustrates the
507 pitfall of using data for only one Th isotope when making inferences about the appropriateness of
508 a Th cycling model.

509 **4.1 Robustness of the Test**

510 **4.1.1 Sensitivity to Vertical Smoothing**

511 In section 3, we tested model V2 using a smoothing parameter $\gamma = 1$. In order to document the
512 effect of γ on our results, we fit model V2 to GT11-22 data (interpolated values obtained using
513 $\sigma_M^2 = 0.5\sigma_d^2$ and $l_z = 1000$ m) using $\gamma = 0.01$ or $\gamma = 100$. For $\gamma = 0.01$, a solution is found
514 after 66 iterations and the model equations are satisfied to the third order. For $\gamma = 100$, a solution
515 is found after 8 iterations and the model equations are also satisfied to the third order. When
516 $\gamma = 0.01$, the fraction of normalized residuals less than 2 in absolute magnitude (ϕ) reaches 0.86,
517 and the bias (B) shrinks to -0.27. When $\gamma = 100$, $\phi = 0.62$ and $B = -0.60$. Thus decreasing γ
518 improves the fit of model V2 to the data, though in each case model V2 displays a better fit to the
519 data than model V1 (see Table 3). The resulting vertical profiles of $(k_1, k_{-1}, \beta_{-1}, w)$ are compared in
520 Figure 12. As expected, the posterior variances in the rate parameters are larger when γ is smaller.
521 Moreover, some β_{-1} and w values are negative if $\gamma = 0.01$. The intermediate value of $\gamma = 1$
522 provides the rate parameters some ability to vary with depth while preventing them from taking on
523 negative values.

524 **4.1.2 Sensitivity to Initial Estimates**

525 In section 3, our initial estimate $\hat{\mathbf{x}}_{k=0}$ was constructed so as to satisfy the measurements and the
526 interpolation assumptions, i.e., $\hat{\mathbf{x}}_{k=0} = \mathbf{x}_0$. However, due to the nonlinearity of $\mathbf{f}(\mathbf{x})$, the ATI
527 may converge to a solution that depends on $\hat{\mathbf{x}}_{k=0}$ (*Tarantola and Valette, 1982*). In particular, with
528 $\mathbf{f}(\mathbf{x})$ being nonlinear, initial estimates of \mathbf{x} that are far from the "true" solution may not lead to
529 this solution but to a secondary minimum of J . Here we examine whether our results hold for a
530 different initial estimate of the state vector, i.e. $\hat{\mathbf{x}}_{k=0} \neq \mathbf{x}_0$. Specifically, $\hat{\mathbf{x}}_{k=0}$ is constructed so

Table 3: Measures of goodness of fit of model V1 and V2 to GT11-22 data for different initial estimate $x_{k=0}$.

	'reference' $\hat{x}_{k=0}$	model-based $\hat{x}_{k=0}$	$\text{Th}_{p,l}/\text{Th}_{p,s}=0.07$	corrected ^{230}Th (a)	QMA bias 20%
ϕ for V1	0.54	0.54	0.53	0.53	0.55
ϕ for V2	0.74	0.73	0.73	0.73	0.76
B for V1	-1.91	-1.91	-1.85	-1.84	-1.64
B for V2	-0.45	-0.40	-0.49	-0.46	-0.38

a.measured $^{230}\text{Th}_{d,p}$ corrected for lithogenic ^{230}Th .

531 as to satisfy the model equations perfectly: the parent activities (^{234}U , ^{238}U , ^{228}Ra), the boundary
532 values of $^{228,230,234}\text{Th}_p$ and P , and the rate parameters are equal to their prior values as in section
533 3, but the other elements of $\hat{x}_{k=0}$ ($^{228,230,234}\text{Th}_{d,p}$ and P at all depths save at the boundary point)
534 are obtained as the solution of the model with these prior values.

535 We find that the results of the inversions for the two different estimates $\hat{x}_{k=0}$ are very similar
536 (Table 3). The ATI converges to a stable solution after 12 iterations and all model equations are
537 satisfied to at least the third order. Model V2 provides a superior fit to the data ($0.73 \leq \phi \leq 0.74$)
538 compared to model V1 ($\phi = 0.54$). The bias of the fit is also similar between both inversions
539 for model V2 ($-0.45 \leq B \leq -0.4$) and both inversions for model V1 ($B = -1.91$). Thus, our
540 test of models V1 and V2 does not depend on whether the initial state estimate satisfies the entire
541 set of prior values, or only a fraction of the prior values and the model equations. This result
542 is encouraging, although we cannot rule out that other plausible choices of $\hat{x}_{k=0}$ would lead to
543 different results.

544 4.1.3 Sensitivity to Bulk Particle Activities

545 Our observational estimates of bulk particulate $^{234,230,228}\text{Th}$ assumed a ratio between large and
546 small particulate Th activities of 0.19 (see section 2.4). This value is large compared to the
547 $^{234}\text{Th}_{p,l}/^{234}\text{Th}_{p,s}$ ratio of 0.07 found by *Buesseler et al. (2001)* in the Southern Ocean. In order
548 to test the effects of a smaller ratio, we repeat our inversion using bulk particulate Th data based on
549 a large to small particulate Th activity of 0.07 (*Buesseler et al., 2001*). We find that, in this case,
550 the model equations are satisfied to the third order, and the objective function again converges after
551 14 iterations. The results are very similar to those of our reference solution (Table 3).

552 **4.1.4 Sensitivity to Lithogenic Sources**

553 Our model does not consider the contribution of a lithogenic source to $^{230}\text{Th}_p$. In order to test the
554 sensitivity of our results to the inclusion of this source, we repeat our inversion by correcting $^{230}\text{Th}_p$
555 data for a contribution from lithogenic material (section 2.5). In this case, we find that the model
556 equations are satisfied to the third order, and the objective function converges after 15 iterations.
557 No notable difference between these results and those from the reference inversion occurs (Table
558 3). Despite the relatively large ($>30\%$) contribution to $^{230}\text{Th}_p$ from lithogenic particles in the upper
559 500 m, the solution is insensitive to this correction, presumably because the lithogenic source is
560 small compared to other sources and sinks of $^{230}\text{Th}_p$.

561 **4.1.5 Sensitivity to Filtering Bias**

562 Finally, we consider the effects of a potential bias due to the filters chosen to extract Th isotopes.
563 *Maiti et al. (2012)* found no significant differences in ^{234}Th activities between different filter types
564 and pore sizes (between 0.2-0.8 μm), except for the quartz filters: the ^{234}Th activities measured on
565 QMA filters were found to be 10% to 20% higher than those measured on Supor filters. The higher
566 activities on QMA filters were attributed mainly to sorption (*Maiti et al., 2012*). In order to test a
567 potential bias due to $^{228,234}\text{Th}$ sorption on QMA filters, we repeat our inversions by reducing the
568 particulate ^{234}Th and ^{228}Th data values by 20%. In this case, the model equations are satisfied to
569 the third order and the objective function converges after 14 iterations. The values of ϕ and B are
570 close to those of our reference solution (Table 3), suggesting our results are not very sensitive to a
571 potential bias due to the use of different types of filters.

572 **4.1.6 Kolmogorov-Smirnov Test**

573 In order to further test whether our results are robust against the changes discussed in sections
574 4.1.2-4.1.5, we employ a Kolmogorov-Smirnov test (Appendix B). The tests show that these
575 changes do not significantly alter the results compared to those of our reference solution (section
576 3).

577 4.2 Implications for Oceanic Th Geochemistry

578 4.2.1 Effect of Particle Concentration

579 In this section, we examine the roles of adsorption (k_1), desorption (k_{-1}), and remineralization
580 (β_{-1}) in the fit of model V2 to GT11-22 data. For simplicity we consider a single parameter, $K =$
581 $k_1/(k_{-1} + \beta_{-1})$. Thus, a value of $K < 1$, for example, would imply that the specific rate at which
582 Th attaches to particles is smaller than those at which it is released from particles by desorption
583 and remineralization. Interestingly, the vertical profile of K in our reference solution (section 3)
584 shows a decrease with depth in the upper 2000 m and relatively uniform values below (Figure 13a).
585 Using data from the Guatemala and Panama Basins, *Bacon and Anderson (1982)* estimated that
586 the k_1/k_{-1} ratio ranged from 0.078 to 0.462, where their k_{-1} included both remineralization and
587 desorption. These values are consistent with our estimates of K at station GT11-22. However,
588 the k_1/k_{-1} ratio of *Bacon and Anderson (1982)* did not show similar variability with depth across
589 stations, so it is unclear whether the profile of K derived here (Figure 13a) is consistent with their
590 findings.

591 We find a higher K value in the upper 2000 m, mainly because k_1 is enhanced in these waters
592 (Figure 9). A potential cause of the increased adsorption rate constant in the upper 2000 m is the
593 higher particle concentration in this region of the water column, because of the increase in the
594 number of surface sites available for attachment (*Honeyman et al., 1988*). We assess the strength
595 of the association between k_1 and P (Figure 14a), as well as between K and P (Figure 14b), using
596 the Kendall tau (τ) rank correlation coefficient (*Kendall and Gibbons, 1990*). This coefficient
597 ranges between -1 and 1 , where a value of 1 (-1) implies a perfect positive (negative) monotonic
598 relationship between k_1 (or K) and P . We find that $\tau = 0.73$ ($p < 0.01$) for the relationship
599 between k_1 and P , and $\tau = 0.70$ ($p < 0.01$) for the relationship between K and P (the Pearson
600 correlation coefficient for both of these relationships amount to $r = 0.89$). Thus both k_1 and K
601 increase significantly with P .

602 *Honeyman et al. (1988)* and *Honeyman and Santschi (1989)* have calculated an equilibrium
603 distribution coefficient, $\bar{K}_D = k_1/(k_{-1}P)$ to describe the affinity of trace metals for particles.

604 Echoing previous studies, [Honeyman et al. \(1988\)](#) found that \overline{K}_D decreases with increasing particle
605 concentration, a phenomenon referred to as the "particle concentration effect". According to these
606 authors, one potential cause for this effect is that the rate of adsorption of trace metals onto filterable
607 particles depends on the rate of coagulation of colloidal ($< 0.8 \mu\text{m}$) particles. They showed that
608 \overline{K}_D should decrease with P , even though k_1 increases with particle concentration, because \overline{K}_D
609 varies explicitly as P^{-1} while k_1 has a power law dependence with particle concentration, $k_1 =$
610 $k_{1,c}P^b$, where $k_{1,c}$ is constant and $b < 1$.

611 We examine the possibility of a particle concentration effect at station GT11-22 from the values
612 of $\overline{K}_{D,\beta-1} = k_1 / ((k_{-1} + \beta_{-1})P)$ obtained from the fit of model V2 to the data gathered at that
613 station. The profile of $\overline{K}_{D,\beta-1}$ shows a general increase with depth (Figure 13b). [Hayes et al.](#)
614 (2015a) estimated $K_D = A_p / (A_d P)$ from ^{230}Th and filtered particle concentration data from the
615 GA03 transect (eq. (3b) shows that A_p / A_d equals $k_1 / (k_{-1} + \beta_{-1})$ if sinking and radioactive decay
616 are neglected). Their method involved dividing ^{230}Th adsorbed onto particles by ^{230}Th in the
617 dissolved phase and normalizing this ratio to the filtered particulate matter concentration (> 0.8
618 μm). Our values for $\overline{K}_{D,\beta-1}$, between 1.5×10^{-5} and $5 \times 10^{-5} \text{ m}^3 \mu\text{g}^{-1}$, are within the range found
619 by [Hayes et al. \(2015a\)](#) below 500 m, from about 1×10^{-5} to about $1 \times 10^{-4} \text{ m}^3 \mu\text{g}^{-1}$. Plotting
620 $\ln(\overline{K}_{D,\beta-1})$ against $\ln(P)$ suggests that, in general, $\overline{K}_{D,\beta-1}$ decreases with P (Figure 14d). The
621 rank correlation between $\ln(\overline{K}_{D,\beta-1})$ and $\ln(P)$ amounts to $\tau = -0.62$ with $p < 0.01$ ($r = -0.75$),
622 which indicates a significant negative monotonic relationship between both variables and hence the
623 possibility of a particle concentration effect. Note that below about 3500 m, the vertical gradient
624 of $\overline{K}_{D,\beta-1}$ is particularly large. However, this feature is due at least partly to the decrease in the
625 estimated particle concentrations below 3500 m, which is not observed (Figure 8).

626 If a particle concentration effect exists, k_1 should vary as P^b , where b is less than 1 (see dashed
627 line in Figure 14a). Conversely, in the absence of such an effect, $\overline{K}_{D,\beta-1}$ should be independent
628 of particle concentration (see dashed line in Figure 14d). A least-squares fit of $\ln(k_1)$ vs. $\ln(P)$
629 yields a slope of 0.60 ± 0.05 . This contrasts with the slope obtained by [Honeyman et al. \(1988\)](#)
630 of 0.51-0.58 from field data spanning a much larger particle concentration range from $O(10^4 \mu\text{g}$

631 m^{-3}) to $O(10^{12} \mu\text{g m}^{-3})$. For the regression of $\ln(\overline{K}_{D,\beta_{-1}})$ against $\ln(P)$, we obtain a slope of
 632 -0.36 ± 0.06 , smaller in magnitude than the slope of -0.42 found by *Honeyman et al. (1988)*
 633 from the same field data used to obtain their $\ln(k_1)$ vs. $\ln(P)$ slope. These results suggest that the
 634 particle concentration effect we obtain from our analysis of station GT11-22 data is not as strong
 635 as that reported by *Honeyman et al. (1988)* for a much larger particle concentration range. This
 636 discrepancy may arise because the particle concentrations reported at station GT11-22 are lower
 637 than those considered by *Honeyman et al. (1988)*. *Honeyman and Santschi (1989)* found that \overline{K}_D
 638 appears independent of particle concentration below $10^4 \mu\text{g m}^{-3}$, a value larger than P at any
 639 depth investigated here. Interestingly, using ^{230}Th activity and particle concentration data across
 640 the entire North Atlantic section, *Hayes et al. (2015a)* found a much larger slope of $\log_{10}(\overline{K}_D)$
 641 vs. $\log_{10}(P)$ of -0.66 ($r^2 = 0.53$). Such a discrepancy may be due to station GT11-22 being
 642 an oligotrophic site with low colloidal concentrations relative to stations closer to the margins.
 643 Nevertheless, our findings suggest that a particle concentration effect does remain present at this
 644 station, albeit reduced compared to the one found at higher particle concentrations.

645 *Bacon and Anderson (1982)* reported that k_{-1} does not depend on particle concentration from
 646 data collected in the Panama and Guatemala Basins. We test whether k_{-1} depends on particle
 647 concentration according to our analysis of GT11-22 data. We find that for the relationship between
 648 $\ln(k_{-1})$ and $\ln(P)$, $\tau = -0.18$ ($p = 0.11$) and the slope of the least squares fit is -0.06 ± 0.04
 649 ($r = -0.19$). Thus, we find no significant evidence that P affects k_{-1} , consistent with *Bacon and*
 650 *Anderson (1982)*.

651 **4.2.2 Vertical Variation in Particle Settling Speed**

652 In this section, we discuss the profile of particle sinking speed obtained from the fit of model
 653 V2 to GT11-22 data. Particle concentration in model V2 shows a decrease below 2000 m that is
 654 not as pronounced as in model V1. Associated with this feature is the inference of relatively large
 655 particle settling speeds below 2000 m. The particle sinking term can be either a loss or a source
 656 in the particle equation (eq. 3c). For example, if there are more particles at the depth above a grid

657 point than at the depth of the grid point, that grid point will "gain" particles from sinking. In this
658 case, increasing the sinking velocity tends to increase the particle concentration and to better offset
659 the loss due to particle remineralization. As a result, particle concentration in deep water is higher
660 in model V2 compared to model V1 (compare Figure 7j to Figure 8j).

661 It is difficult to determine possible mechanisms underlying the vertical variation in our particle
662 sinking speed profile, in particular because our model does not discriminate between large and
663 small particles. One of the most noticeable features in this profile is an apparent increase in sinking
664 speed below 2000 m. One potential cause for the apparent increase in particle sinking speed is a
665 local increase in the rate of aggregation of suspended particles, resulting in an increase in large,
666 more quickly sinking particles and hence in bulk w . However, this appears unlikely given the
667 nearly constant partitioning of particles between the small and large size fractions below 2000 m at
668 station GT11-22 ([Lam et al., 2015](#)). The apparent increase in particle sinking speed may reflect a
669 bias due to the exclusion of other processes that could increase particle concentration below 2000
670 m, such as lateral transport of suspended particles.

671 Below 2000 m, the particle sinking speed inferred by inversion exhibits significant variability
672 on short vertical scales (Fig. 10). Interestingly, similar variability is not apparent in the inferred
673 vertical profiles of the parent isotope activities, Th isotope activities, and particle concentration.
674 Below 2000 m, the particle sinking term is a minor term in the balance of the particulate Th isotopes
675 (Section 4.3), except for $^{228}\text{Th}_p$. Speculatively, the large variability of w at small vertical scales
676 would be due to the small vertical gradients of particulate $^{228}\text{Th}_p$ between about 2000 and 3500 m:
677 small changes in these gradients would require large changes in w to achieve a balance between the
678 particulate $^{228}\text{Th}_p$ sources and sinks at different levels within this depth interval. Whereas further
679 inversions may help to isolate the specific measurements that are responsible for the inference of a
680 large variability of w below 2000 m, such effort is beyond the scope of this study.

681 To our knowledge, there are no reported depth-varying estimates of the sinking speed of bulk
682 particles (small + large) in the current literature. [Armstrong et al. \(2009\)](#) and [Lee et al. \(2009\)](#)
683 collected sinking particles using indented rotating-sphere settling velocity (IRS-SV) traps placed

684 at various depths at a location in the northwestern Mediterranean Sea. These traps have the ability
685 to sort the mass flux density of particles into sinking speed bins. The mass flux density is defined as
686 the mass of any constituent per square meter of trap area, integrated over the trap deployment time
687 and divided by $\log_{10}(SV_{max}/SV_{min})$, where $SV_{max}(SV_{min})$ is the maximum (minimum) particle
688 settling speed in a given SV range. *Armstrong et al. (2009)* and *Lee et al. (2009)* found that, at all
689 depths, (i) the majority of the mass flux density of particles occurs within a rapidly sinking (200–
690 500 m d⁻¹) speed interval, and (ii) the mass flux density presents an exponential "tail" within a
691 much slower (0.68-2.7 m d⁻¹) sinking speed interval. Closer to station GT11-22, *Alonso-González*
692 *et al. (2010)* conducted a study south of the Canary Islands using IRS-SV traps placed at a depth
693 of 260 m. They found that the mass flux density was highest in the low sinking speed range (0.7-
694 11 m d⁻¹), which overlaps with the range of sinking speeds obtained from the fit of model V2
695 to GT11-22 data (0.19-3.86 m d⁻¹). Therefore, it could be concluded that the vast majority of
696 particles below 125 m at station GT11-22 settle very slow. However, comparison to our study is
697 difficult. Whereas *Armstrong et al. (2009)*, *Lee et al. (2009)*, and *Alonso-González et al. (2010)*
698 consider particles within specific sinking speed ranges, the sinking speeds reported here are average
699 values for the bulk particle concentration (all particles) at a given depth. The sinking speeds of the
700 different particles may vary greatly, making the interpretation of our estimated sinking speeds
701 difficult. Therefore, caution must be applied when comparing our bulk particle sinking speeds to
702 those obtained from sediment or settling velocity traps.

703 **4.3 Diagnosis of Th Isotope Budgets**

704 In this section, we examine the budget of each Th isotope at station GT11-22, as determined by
705 inversion of the particle and radiochemical data. The different terms of the budget are, for each Th
706 isotope, the adsorption flux ($k_1 A_d$), the desorption flux ($k_{-1} A_p$), the remineralization flux ($\beta_{-1} A_p$),
707 the particle sinking flux ($w \partial A_p / \partial z$), the decay fluxes (λA_d , λA_p), and the production flux (λA_π).
708 Since our estimation of the flux terms accounts for the data uncertainties but not for the model
709 uncertainties, it should only be considered as suggestive.

710 4.3.1 ^{234}Th

711 The dominant terms in the $^{234}\text{Th}_d$ budget (Figure 15) are the production and decay terms. These
712 terms are the largest because $^{234}\text{Th}_d$ and ^{238}U are one order of magnitude larger than $^{234}\text{Th}_p$, and
713 the decay constant for ^{234}Th is about one order of magnitude larger than k_1 , k_{-1} , and β_{-1} . For the
714 $^{234}\text{Th}_p$ budget, the first-order terms are the adsorption flux and radioactive decay. The adsorption
715 term dominates because it includes $^{234}\text{Th}_d$, and the decay term is the main loss because the decay
716 constant is much larger than the other rate constants. The particle sinking term is particularly small
717 below 800 m, where $^{234}\text{Th}_p$ shows small vertical variations (Figure 5). The average fluxes, taken by
718 integrating the source and loss terms and dividing by the vertical extent of our domain (from 125 to
719 4243 m), are shown in Figure 15a. To obtain kinetic measures in the budget, we calculate residence
720 times by dividing the depth-averaged Th isotope activity by the dominant depth-averaged volumet-
721 ric flux associated with that isotope. We find that the residence time with respect to radioactive
722 production is 34 days for $^{234}\text{Th}_d$, and the residence time with respect to adsorption is 29 days for
723 $^{234}\text{Th}_p$.

724 4.3.2 ^{228}Th

725 Unlike for $^{234}\text{Th}_d$, the dominant terms in the $^{228}\text{Th}_d$ budget vary with depth. Near the surface,
726 radioactive production is the dominant source, and is balanced mostly by adsorption of $^{228}\text{Th}_d$.
727 However, throughout most of the water column, adsorption, decay, desorption, and production are
728 nearly equivalent in magnitude. Below 3500 m, adsorption and decay are comparable as losses of
729 $^{228}\text{Th}_d$, and production once again becomes the dominant source. This pattern is consistent with
730 the vertical profile of ^{228}Ra , which has surface and deepwater maxima and is minimum near the
731 middle of the water column. Thus production is highest in near-surface and deep waters. Near the
732 surface, the adsorption term is larger than decay of $^{228}\text{Th}_d$, even though both scale with $^{228}\text{Th}_d$,
733 because k_1 is highest in surface waters (Figure 10).

734 The dominant terms in the $^{228}\text{Th}_p$ budget similarly vary with depth. Near the shallowest depth,
735 adsorption is the dominant source, balanced mostly by desorption. Near the surface, the particle

736 sinking flux is a loss term for $^{228}\text{Th}_p$, but becomes a source equivalent in magnitude to adsorption
737 below about 500 m. Below about 3500 m, $^{228}\text{Th}_p$ is lost in about equal measure through particle
738 sinking and desorption, and is gained solely through adsorption. We show the average fluxes for
739 $^{228}\text{Th}_{d,p}$ in Figure 16a. The residence time of $^{228}\text{Th}_d$ and $^{228}\text{Th}_p$ with respect to adsorption is 891
740 days (2.44 yr) and 125 days, respectively.

741 **4.3.3 ^{230}Th**

742 Since the radioactive decay constant for ^{230}Th is about 5 orders of magnitude smaller than the
743 rate parameters k_1 , k_{-1} , and β_{-1} , production and decay generally no longer dominate the budget
744 for the dissolved and particulate phases. Instead, desorption is the first-order source of $^{230}\text{Th}_d$ and
745 adsorption is the first-order loss, with production and remineralization being second-order gains
746 except nearest to the surface. The primary mechanisms influencing $^{230}\text{Th}_p$ are also adsorption and
747 desorption, with remineralization and sinking being generally losses of second-order importance.
748 We show the average fluxes for $^{230}\text{Th}_{d,p}$ in Figure 17a. The residence time of $^{230}\text{Th}_d$ and $^{230}\text{Th}_p$
749 with respect to adsorption is 1090 days (2.98 yr) and 130 days, respectively.

750 **4.4 Interpretation of Particle and Th isotope residuals**

751 **4.4.1 Model with Uniform Rate Parameters**

752 The values of $^{234}\text{Th}_d$ estimated from the fit of model V1 to GT11-22 data show vertical variations
753 associated with vertical variations in ^{238}U (Figure 7). Some of the ^{238}U values inferred from the
754 fit differ from prior values estimated from salinity by more than one standard deviation. These
755 values seem to stem from the attempt by the algorithm to produce the best fit to the $^{234}\text{Th}_d$ data:
756 since rate parameters cannot vary with depth in model V1, the algorithm allows the parent isotope
757 to change in order to fit the daughter. In any case, it is clear that model V1 cannot fit uranium
758 and thorium activities very well (e.g. Figure 7e), with the exception of ^{228}Th and ^{228}Ra . Unlike
759 the $^{238,234}\text{U}$ estimates derived from salinity, ^{228}Ra measurements show consistent variability with
760 depth (maxima in near surface and deep waters, minima at mid-depth), which is largely reflected in
761 the $^{228}\text{Th}_d$ and $^{228}\text{Th}_p$ data. Therefore, whereas the algorithm produces $^{234,238}\text{U}$ values that deviate

762 significantly from prior estimates, such large deviations from the prior estimates are generally not
763 as necessary for ^{228}Ra to reach consistency with the model. Finally, the particle concentrations
764 inferred by inversion show an exponential decrease with depth, in contrast to the data which shows
765 a slight increase below 2000 m. Below this depth, model V1 is unable to replicate the particle data
766 within two standard deviations (Figure 7).

767 4.4.2 Model with Non-Uniform Rate Parameters

768 Model V2 produces enhanced agreement with radiochemical and particle data from station
769 GT11-22 (Figure 8). This can be viewed most clearly by the much improved fit of model V2
770 to $^{234,238}\text{U}$, $^{230}\text{Th}_d$, and particle data. However, even allowing the rate parameters to vary with
771 depth does not allow the model to fit the entire data set. In particular, $^{234}\text{Th}_d$, $^{230}\text{Th}_p$, and parti-
772 cle concentration contain regions of relatively large normalized residuals (Figure 8). The vertical
773 variations in the $^{234}\text{Th}_{tot}$ data (used to derive $^{234}\text{Th}_d$) are large compared to those in the salinity-
774 based estimates of ^{238}U (compare Figure 5a with Figure 5b). The half-life of $^{234}\text{Th}_d$ (24.1 days)
775 implies that processes responsible for departure from secular equilibrium should be characterized
776 by a timescale of a few weeks or less. It is worthwhile to note that such departures from secular
777 equilibrium in deep-water $^{234}\text{Th}_{tot}$ are not unique to station GT11-22. *Owens et al. (2015)* have
778 shown how $^{234}\text{Th}_{tot}$ disequilibrium is prevalent in deep waters throughout the section. For instance,
779 cross-over station GT11-24 (Figure 1) exhibits $^{234}\text{Th}_{tot}$ deficits, while station GT22-20 (the second
780 station to the west of GT11-22; Figure 1) exhibits $^{234}\text{Th}_{tot}$ excess, like station GT11-22. While a
781 subsurface excess in $^{234}\text{Th}_{tot}$ relative to secular equilibrium may be explained by a deficit in ^{234}Th
782 in the surface due to enhanced scavenging and subsequent remineralization of Th-laden particles
783 just beneath the surface (*Maiti et al., 2015*), a mechanism for maintaining a $^{234}\text{Th}_{tot}$ excess be-
784 low 1000 m has yet to be elucidated. Therefore, the variations in $^{234}\text{Th}_{d,tot}$ remain a confounding
785 element of the GEOTRACES North Atlantic data set.

786 On the other hand, ^{230}Th appears more likely to be influenced by the transport of water masses.
787 Due to its long half-life, ^{230}Th anomalies can be transported over large distances in the ocean,

788 provided that these anomalies are not erased by the effects of particle scavenging and water mix-
789 ing. For example, ventilation by $^{230}\text{Th}_d$ -poor water from the northern North Atlantic has been
790 postulated to influence ^{230}Th in deep water in the North Atlantic (*Moran et al., 1997; Vogler et al.,*
791 *1998*). Here, we examine the potential influence of two water masses, Upper Labrador Sea Wa-
792 ter (ULSW) and Central Labrador Sea Water (CLSW), on the misfits of model V2 to ^{230}Th data
793 for station GT11-22. Figure 18 compares the normalized $^{230}\text{Th}_d$ and $^{230}\text{Th}_p$ residuals with the
794 estimated proportion of ULSW and CLSW at this station (*Jenkins et al., 2015*). Since LSW is
795 characterized by low $^{230}\text{Th}_d$ (*Moran et al., 2002*), an intrusion of LSW at station GT11-22 should
796 be reflected in low $^{230}\text{Th}_d$ activities between 1500 and 3000 m. Such an intrusion would also re-
797 sult in low $^{230}\text{Th}_p$ if $^{230}\text{Th}_d$ continuously undergoes reversible exchange in transit. However, the
798 $^{230}\text{Th}_d$ normalized residuals are only large (and negative) in the top 500 m, and do not show any
799 systematic change below 1500 m, where Labrador Sea Waters are inferred to be present (section
800 2.1). Therefore, it seems unlikely that the $^{230}\text{Th}_{d,p}$ residuals arise from the omission of the effect of
801 LSWs in the model. Other processes missing in model V2 must be responsible for the significant
802 $^{230}\text{Th}_{d,p}$ residuals (see section 2.4 for model limitations).

803 Both model V1 and V2 underpredict particle concentrations compared to observations below
804 2000 m. Since our interpolation grid only extends down to 4243 m, only 2 measurements of parti-
805 cle concentration were considered in the data interpolation below 2000 m. Inspection of the entire
806 particle concentration profile from 125 m to 4989 m (Figure 19) confirms that particle concen-
807 tration remained constant or increased slightly with depth below 2000 m, consistent with beam
808 attenuation coefficient data at station GT11-22 (*Anderson et al., 2013*). Although a slight bottom
809 nepheloid layer might have been present at station GT11-22, as was observed at other stations
810 along the section (*Lam et al., 2015*), the particle residuals below 2000 m (Figure 19) should proba-
811 bly not be interpreted as due to the omission of such a layer in the model. Another potential source
812 of misfit of model V2 to particle concentration data is lateral transport of suspended particles
813 (*Alonso-González et al., 2010*), although it is unclear whether there can be particle enriched wa-
814 ters moving laterally to station GT11-22 below 2000 m. *McCartney et al. (1991)* and *Schmitz and*

815 *McCartney (1993)* have presented a schematic of the AABW circulation in the North Atlantic in
816 which the bottom water flowing through the Vema Fracture Zone enters the eastern North Atlantic
817 basins and becomes part of the NADW. Speculatively, this water may be enriched in suspended
818 particles due to intense turbulent mixing within the fracture zone (*Polzin et al., 1996; Hayes et al.,*
819 *2015b*).

820 Finally, notice that we have not shown that model V2 is a "good" model, in the sense that it
821 is both parsimonious with parameters and does not over-fit the data. Rather our study evaluates
822 whether the mere allowance of vertical variations in model parameters, with no change in model
823 structure (e.g., assumption of second-order instead of first-order kinetics for Th adsorption flux)
824 and with no additional terms in the model (e.g., horizontal transport), can significantly improve the
825 fit to radiochemical and particle data for an open-ocean station. We show that a significantly better
826 fit is obtained in this case (in fact, model V2 leads generally to an over-fit compared to the normal
827 distribution) and, moreover, that some of the inferred parameters may feature systematic vertical
828 variations suggestive of a particle concentration effect in situ.

829 **5 Conclusion**

830 A suite of radiochemical and particle data from station GT11-22 of the U.S. GEOTRACES
831 North Atlantic section are used to test two versions of a particle and Th cycling model that assumes
832 a single class of particles. Model V2, with depth-dependent rate parameters, shows a significant
833 improvement in fit to the data set than model V1 with uniform rate parameters. In contrast to the
834 reversible exchange model described by *Bacon and Anderson (1982)*, we are able to successfully
835 tease apart desorption (k_{-1}) and remineralization (β_{-1}) by invoking a model that describes thorium
836 as well as particle cycling in the deep ocean. We find that k_{-1} is much larger than β_{-1} , suggesting
837 that remineralization does not result in a major loss of particulate thorium. Our analysis illustrates
838 the pitfall of using data for a single Th isotope when testing particle and Th cycling models. It
839 suggests the occurrence of systematic vertical variations in some of the rate constants (most notably
840 k_1 and w) and in some of their combinations ($K = k_1/(k_{-1} + \beta_{-1})$ and $\overline{K}_{D,\beta_{-1}} = K/P$) in the
841 mesopelagic and bathypelagic zones. It points to a significant effect of particle concentration on

842 K and K/P in situ, i.e., k_1 and K increase with P whereas K/P decreases with P . Finally,
843 it suggests that deviations of Th profiles from those predicted by reversible exchange, which are
844 often interpreted in terms of an effect of ocean circulation, could be due, at least partly, to vertical
845 variations in rate constants.

846 While model V2 can describe most of the GT11-22 data, it does not explain the entire data set.
847 Features in the data that remain unexplained by model V2 include the large vertical variations of
848 total (and hence dissolved) ^{234}Th , the kink in the particulate ^{230}Th profile near 2000 m, and the
849 relatively uniform particle concentration below that depth. Finally, one should exercise caution
850 when interpreting the rate parameters obtained from this study. The parameters we estimate are
851 apparent ones that may, at least partially, mask the effects of processes not encapsulated in the
852 model used here. We cannot rule out the presence of a bias in the inferred rate parameters, because
853 the processes not described by the model may be the source of systematic errors. The fact that we
854 can produce a reasonable fit to station GT11-22 data does not imply that there is no influence from
855 other processes, such as the circulation of deep water masses, on the isotope activities and (or)
856 particle concentrations. The parameter estimated obtained in this study are only as reliable as the
857 assumptions about the data errors (C_0) and parameter distribution (S) from which these estimates
858 have been derived.

859 **Acknowledgement**

860 We acknowledge the U.S. National Science Foundation for providing funding for this study
861 (grant OCE-1232578) and for U.S. GEOTRACES North Atlantic section ship time, sampling,
862 and data analysis. The U.S. NSF also supported the generation of ^{230}Th data (OCE-0927064 to
863 LDEO, OCE-0092860 to WHOI, and OCE-0927754 to UMN) and $^{228,234}\text{Th}$ data (OCE-0925158
864 to WHOI). We thank the two chief scientists of the GA03 section (Ed Boyle and Bill Jenkins)
865 as well as the captain, the crew, and the scientific party on the R/V Knorr, which completed this
866 section. We are also grateful to the scientists and staff involved in the collection and analysis of
867 the thorium isotope and particle data.

Table A.1: Radiochemical and Particle Concentration Data at Station GT11-22

depth (m)	U	²²⁸ Ra	²³⁴ Th _{tot}	²³⁴ Th _{p,s}	²³⁴ Th _{p,l}	²³⁰ Th _d	²³⁰ Th _{p,s}	²²⁸ Th _d	²²⁸ Th _{p,s}	P _s	P _l	reference
1,25,49	✓		✓									a
50		✓		✓	✓	✓		✓	✓	✓	✓	a, b, c, d
75						✓						b
84						✓						b
90		✓		✓	✓			✓	✓	✓	✓	a, c, d
124						✓						b
125	✓	✓	✓	✓	✓		✓	✓	✓	✓	✓	a, b, c, d
149	✓		✓									a
184						✓						b
185	✓		✓									a
187		✓		✓	✓			✓	✓			a, c
233						✓						b
234	✓		✓									a
237		✓		✓	✓		✓	✓	✓	✓	✓	a, b, c, d
283						✓						b
285,389	✓		✓									a
392		✓		✓	✓			✓	✓	✓	✓	a, c, d
549	✓		✓									a
551		✓		✓	✓			✓	✓	✓	✓	a, c, d
568,663						✓						b
664	✓		✓									a
751	✓		✓									a
896	✓		✓									a
897		✓		✓	✓		✓	✓	✓	✓	✓	a, b, c, d
898,1195						✓						b
1351	✓		✓									a
1492						✓						b
1498		✓		✓			✓	✓	✓			a, b, c
1793,2092						✓						b
2098		✓		✓			✓	✓	✓	✓	✓	a, b, c, d
2251,2851	✓		✓									a
2988		✓				✓		✓	✓			b, c
2998				✓			✓					a, b
3451	✓		✓									a
3568						✓						b
3600		✓		✓			✓	✓	✓	✓	✓	a, b, c, d
3851,4051	✓		✓									a
4184						✓						b
4200		✓		✓			✓	✓	✓			a, b, c
4243	✓		✓									a
4581						✓						b
4600		✓		✓			✓	✓	✓	✓	✓	a, b, c, d
4802		✓		✓			✓	✓	✓			a, b, c
4970						✓						b
4989		✓		✓			✓	✓	✓	✓	✓	a, b, c, d

a. ²³⁴Th data from *Owens et al. (2015)*

b. ²³⁰Th data from *Anderson et al. (2012)*; *Hayes et al. (2015b)*.

c. ²²⁸Th data from *Charette et al. (2015)*

d. Particle concentration data from *Lam et al. (2015)*

869 **B Appendix B**

870 We use a Kolmogorov-Smirnov (KS) test (*Dudewicz and Mishra, 1988*) in order to test the null
 871 hypothesis that the results of our reference solution (section 3) are not significantly different from
 872 the results derived from the changes discussed in sections 4.1.2-4.1.5. The two-sample KS test
 873 compares the maximum vertical distance between two empirical distribution functions (DFs). This
 874 distance is used to construct the probability (p value) of rejecting a null hypothesis that is correct.
 875 The p values for each test are reported in Table B.1.

Table B.1: p values from Kolmogorov-Smirnov test.

	model-based $\hat{x}_{k=0}$	$\text{Th}_{p,l}/\text{Th}_{p,s} = 0.07$	corrected ^{230}Th (a)	QMA bias 20%
p for V1	> 0.99	> 0.99	> 0.99	0.98
p for V2	> 0.99	0.52	> 0.99	0.02

a. measured $^{230}\text{Th}_{d,p}$ corrected for lithogenic ^{230}Th .

876 With one exception, the p values all show that the two considered solutions are not significantly
 877 different. The exception is the test between our reference solution and the solution obtained from
 878 correcting for a potential bias in the QMA filters. Although the KS test suggests that the normalized
 879 residuals of the fit of model V2 to GT11-22 data do not have the same underlying distribution at
 880 the 5% significance level ($p = 0.02$), the DFs of the two solutions look very similar (Figure B.1).
 881 Thus, in fact, the solution with reduced $^{234,228}\text{Th}_p$ data values and the reference solution generally
 882 lead to similar results, in particular regarding the relative merits of model V1 and V2 (Table 3).

883 **References**

884 Alonso-González, I. J., J. Arístegui, C. Lee, A. Sanchez-Vidal, A. Calafat, J. Fabrés, P. Sangrá,
885 P. Masqué, A. Hernández-Guerra, and V. Benítez-Barrios (2010), Role of slowly settling parti-
886 cles in the ocean carbon cycle, *Geophysical Research Letters*, *37*, 1–5.

887 Andersen, M. B., C. H. Stirling, B. Zimmermann, and A. N. Halliday (2010), Precise determination
888 of the open ocean $^{234}\text{U}/^{238}\text{U}$ composition, *Geochemistry, Geophysics, Geosystems*, *11*(12).

889 Anderson, R. F., M. Q. Fleisher, L. F. Robinson, R. L. Edwardds, J. Hoff, S. B. Moram, M. Rutgers
890 van der Loeff, A. L. Thomas, M. Roy-Barman, and R. François (2012), GEOTRACES intercal-
891 ibration of ^{230}Th , ^{232}Th , ^{231}Pa , and prospects for ^{10}Be , *Limnology and Oceanography Methods*,
892 *10*, 179–213.

893 Anderson, R. F., M. Q. Fleisher, and C. Hayes (2013), Transmissometer_GTC,
894 *Biological and chemical oceanography data system*, BCO DMO, WHOI, [http:
895 //data.bco-dmo.org/jg/info/BCO/GEOTRACES/NorthAtlanticTransect/
896 Transmissometer_GTC%7Bdir=data.bco-dmo.org/jg/dir/BCO/
897 GEOTRACES/NorthAtlanticTransect/,data=data.bco-dmo.org:
898 80/jg/serv/BCO/GEOTRACES/NorthAtlanticTransect/GT10-11_trans_
899 Cp_GTC.html0%7D?](http://data.bco-dmo.org/jg/info/BCO/GEOTRACES/NorthAtlanticTransect/Transmissometer_GTC%7Bdir=data.bco-dmo.org/jg/dir/BCO/GEOTRACES/NorthAtlanticTransect/,data=data.bco-dmo.org:80/jg/serv/BCO/GEOTRACES/NorthAtlanticTransect/GT10-11_trans_Cp_GTC.html0%7D?), accessed: 22 January, 2015.

900 Armstrong, R. A., M. L. Peterson, C. Lee, and S. G. Wakeham (2009), Settling velocity spectra
901 and the ballast ratio hypothesis, *Deep Sea Research II*, *56*, 1470–1478.

902 Athias, V., P. Mazzega, and C. Jeandel (2000a), Selecting a global optimization method to estimate
903 the oceanic particle cycling rate constants, *Journal of Marine Research*, *58*(5), 675–707.

904 Athias, V., P. Mazzega, and C. Jeandel (2000b), Nonlinear Inversions of a Model of the Oceanic
905 Dissolved-Particulate Exchanges, *Inverse Methods in Global Biogeochemical Cycles* (eds. P.
906 Kasibhatla, M. Heimann, P. Raynar, M. Mahowald, R. G.Prinn, and D. E. Hartley), Geophysical
907 Monograph, *114*, Am. Geophys. Union. 205–222.

- 908 Bacon, M. P., and R. F. Anderson (1982), Distribution of thorium isotopes between dissolved and
909 particulate forms in the deep sea, *Journal of Geophysical Research: Oceans (1978 to 2012)*,
910 87(C3), 2045–2056.
- 911 Bevington, P. R., and D. K. Robinson (1992), *Data Reduction and Error Analysis for the Physical*
912 *Sciences*, McGraw-Hill, New York.
- 913 Bhat, S. G., S. Krishnaswami, D. Lal, and W. S. Moore (1969), ^{234}Th and ^{238}U ratios in the ocean,
914 *Earth and Planetary Science Letters*, 5, 483–491.
- 915 Bishop, J. K. (2009), Autonomous observations of the ocean biological carbon pump, *Oceanog-*
916 *raphy*, 22(2), 182–193.
- 917 Bishop, J. K., P. J. Lam, and T. J. Wood (2012), Getting good particles: Accurate sampling of
918 particles by large volume insitu filtration, *Limnology and Oceanography: Methods*, 10(9), 681–
919 710.
- 920 Boyle, E. A., R. F. Anderson, G. A. Cutter, R. Fine, W. J. Jenkins, and M. Saito (2015), Introduction
921 to the US GEOTRACES North Atlantic Transect (GA-03): USGT10 and USGT11 cruises, *Deep*
922 *Sea Research Part II: Topical Studies in Oceanography*, 116, 11–5.
- 923 Buesseler, K., L. Ball, J. Andrews, J. Cochran, D. Hirschberg, M. Bacon, A. Flerer, and M. Brzezinski
924 (2001), Upper ocean export of particulate organic carbon and biogenic silica in the Southern
925 Ocean along 170°W, *Deep-Sea Research Part II: Topical Studies in Oceanography*, 48(19),
926 4275–4297.
- 927 Burd, A. B., S. B. Moran, and G. A. Jackson (2000), A coupled adsorption aggregation model of
928 the POC/ ^{234}Th ratio of marine particles., *Deep Sea Research Part I: Oceanographic Research*
929 *Papers*, 47(1), 103–120.
- 930 Charette, M. A., P. J. Morris, P. B. Henderson, and W. S. Moore (2015), Radium isotope Distribu-
931 tions during the U.S. GEOTRACES North Atlantic cruises, *Marine Chemistry*, 177, 184–195.

932 Chen, J. H., L. R. Edwards, and G. J. Wasserburg (1986), ^{238}U , ^{234}U and ^{232}Th in seawater, *Earth*
933 *and Planetary Science Letters*, 80, 241–251.

934 Cheng, H., R. L. Edwards, C. Shen, V. J. Polyak, Y. Asmerom, J. Woodhead, J. Hellstrom, Y. Wang,
935 X. Kong, C. Spötl, X. Wang, and E. C. Alexandar Jr. (2013), Improvements in ^{230}Th dating,
936 ^{230}Th and ^{234}U half-life values, and U-Th isotopic measurements by multi-collector inductively
937 coupled plasma mass spectrometry., *Earth and Planetary Science Letters*, 371, 82–91.

938 Clegg, S. L., and M. Whitfield (1990), A generalized model for the scavenging of trace metals in
939 the open ocean I. Particle cycling, *Deep Sea Research Part A. Oceanographic Research Papers*,
940 37(5), 809–832.

941 Clegg, S. L., M. P. Bacon, and M. Whitfield (1991), Application of a generalized scavenging
942 model to thorium isotope and particle data at equatorial and high-latitude sites in the Pacific
943 Ocean, *Journal of Geophysical Research: Oceans (1978 to 2012)*, 962(C11), 20,655–20,670.

944 Cochran, J. K., K. O. Buesseler, M. P. Bacon, H. W. Wang, D. J. Hirschberg, L. Ball, and A. Flerer
945 (2000), Short-lived thorium isotopes (^{234}Th , ^{228}Th) as indicators of POC export and particle cy-
946 cling in the Ross Sea, Southern Ocean., *Deep Sea Research Part II: Topical Studies in Oceanog-*
947 *raphy*, 47(15), 3451–3490.

948 Cochran, K. J., K. O. Buesseler, M. P. Bacon, and H. D. Livingston (1993), Thorium isotopes
949 as indicators of particle dynamics in the upper ocean: Results from the JGOFS North Atlantic
950 Bloom Experiment., *Deep Sea Research Part I: Oceanographic Research Papers*, 40(8), 569–
951 1595.

952 Delanghe, D., E. Bard, and B. Hamelin (2002), New TIMS constraints on the uranium-238 and
953 uranium-234 in seawaters from the main ocean basins and the Mediterranean Sea, *Marine Chem-*
954 *istry*, 80(1), 79–93.

955 Dudewicz, E. J., and S. N. Mishra (1988), *Modern Mathematical Statistics*, John Wiley and Sons,
956 Inc.

957 Edmonds, H. N., S. B. Moran, J. A. Hoff, J. N. Smith, and R. L. Edwards (1998), Protactinium-231
958 and thorium-230 abundances and high scavenging rates in the western Arctic Ocean, *Science*,
959 280(5362), 405–407.

960 Efron, B., and R. J. Tibshirani (1993), *An introduction to the bootstrap*, Chapman and Hall, New
961 York.

962 François, R., M. Frank, M. M. Rutgers van der Loeff, and M. P. Bacon (2004), ^{230}Th normalization:
963 An essential tool for interpreting sedimentary fluxes during the late Quaternary, *Paleoceanogra-*
964 *phy*, 19(1).

965 Goldberg, E. D. (1954), Marine geochemistry 1. Chemical scavengers of the sea, *The Journal of*
966 *Geology*, pp. 249–265.

967 Hayes, C. T., R. F. Anderson, S. L. Jaccard, R. François, M. Q. Fleisher, M. Soon, and R. Ger-
968 sonde (2013), A new perspective on boundary scavenging in the North Pacific Ocean, *Earth and*
969 *Planetary Science Letters*, 369, 86–97.

970 Hayes, C. T., R. F. Anderson, M. Q. Fleisher, S. W. Vivancos, P. J. Lam, D. C. Ohnemus, K. F.
971 Huang, L. F. Robinson, Y. Lu, H. Cheng, R. L. Edwards, and B. S. Moran (2015a), Intensity
972 of Th and Pa scavenging partitioned by particle chemistry in the North Atlantic Ocean, *Marine*
973 *Chemistry*, 170, 49–60.

974 Hayes, C. T., R. F. Anderson, M. Q. Fleisher, K. F. Huang, L. F. Robinson, Y. Lu, H. Cheng, L. R.
975 Edwards, and B. S. Moran (2015b), ^{230}Th and ^{231}Pa on GEOTRACES GA03, the U.S. GEO-
976 TRACES North Atlantic transect, and implications for modern and paleoceanographic chemical
977 fluxes, *Deep Sea Research Part II: Topical Studies in Oceanography*, 116, 29–41.

978 Henderson, P. B., P. J. Morris, W. S. Moore, and M. A. Charette (2013), Methodological advances
979 for measuring low-level radium isotopes in seawater, *Journal of Radioanalytical and Nuclear*
980 *Chemistry*, 296(1), 357–362.

- 981 Honeyman, B. D., and P. H. Santschi (1989), A Brownian-pumping model for oceanic trace metal
982 scavenging: evidence from Th isotopes, *Journal of Marine Research*, 47(4), 951–992.
- 983 Honeyman, B. D., L. S. Balistrieri, and J. W. Murray (1988), Oceanic trace metal scavenging:
984 the importance of particle concentration, *Deep Sea Research Part A. Oceanographic Research*
985 *Papers*, 35(2), 227–246.
- 986 Jenkins, W. J., W. M. Smethie, and E. A. Boyle (2015), Water mass analysis for the U.S. GEO-
987 TRACES North Atlantic Sections, *Deep Sea Research Part II: Topical Studies in Oceanography*,
988 116, 6–20.
- 989 Kendall, M., and J. D. R. Gibbons (1990), *Rank Correlation Methods*, Oxford University Press,
990 Oxford.
- 991 Kirby, H. W., G. R. Grove, and D. L. Timma (2002), Neutron-capture cross section of actinium-
992 227, *Physical Review*, 102(4), 1140–1141.
- 993 Knight, G. B., and R. L. Macklin (1948), Half-Life of UX_1 (Th_{234}), *Physical Review*, 74(10),
994 1540–1541.
- 995 Krauskopf, K. B. (1956), Factors controlling the concentrations of thirteen rare metals in sea-water,
996 *Geochimica et Cosmochimica Acta*, 9(1), 1–B32.
- 997 Krishnaswami, S., D. Lal, B. L. K. Somayajulu, R. F. Weiss, and H. Craig (1976), Large-volume
998 in-situ filtration of deep Pacific waters: Mineralogical and radioisotope studies, *Earth and Plan-*
999 *etary Science Letters*, 32(2), 1–B32.
- 1000 Krishnaswami, S., M. M. Sarin, and B. L. K. Somayajulu (1981), Chemical and radiochemical
1001 investigations of surface and deep particles of the Indian Ocean, *Earth and Planetary Science*
1002 *Letters*, 51(1), 81–96.
- 1003 Ku, T. L., K. G. Knauss, and G. G. Mathieu (1977), Uranium in open ocean: concentration and
1004 isotopic composition, *Deep Sea Research*, 24(12), 31–39.

- 1005 Kumar, N., R. Gwiazda, R. Anderson, and P. Froelich (1993), $^{231}\text{Pa}/^{230}\text{Th}$ ratios in sediments as a
1006 proxy for past changes in Southern Ocean productivity, *Nature*, 362(6415), 45–48.
- 1007 Kumar, N., R. Anderson, R. Mortlock, P. Froelich, P. Kubik, B. Dittrich-Hannen, and M. Suter
1008 (1995), Increased biological productivity and export production in the glacial Southern Ocean,
1009 *Nature*, 378(6558), 675–680.
- 1010 Lam, P., and O. Marchal (2014), Insights into particle dynamics from the geochemical composition
1011 of suspended and sinking particles, *Annual Review of Marine Science*, 7(1), 12.1–12.26.
- 1012 Lam, P. J., D. C. Ohnemus, and M. E. Auro (2015), Size-fractionated major particle composi-
1013 tion and concentrations from the U.S. GEOTRACES North Atlantic Zonal Transect, *Deep-Sea*
1014 *Research II*, 116, 303–320.
- 1015 Lee, C., M. A. Peterson, S. G. Wakeham, R. A. Armstrong, J. K. Cochran, J. C. Miquel, S. W.
1016 Fowler, D. Hirschberg, A. Beck, and J. Xue (2009), Particulate organic matter and ballast fluxes
1017 measured using time-series and settling velocity sediment traps in the northwestern Mediter-
1018 ranean Sea, *Deep Sea Research II*, 56, 1420–1436.
- 1019 Maiti, K., K. O. Buesseler, S. M. Pike, C. Benitez-Nelson, P. Cai, W. Chen, K. Cochran, M. Dai,
1020 F. Dehairs, B. Gasser, R. P. Kelley, P. Masque, L. A. Miller, J. C. Miquel, S. B. Moran, P. J. Mor-
1021 ris, F. Peine, F. Planchon, A. A. Renfo, M. Rutgers van der Loeff, P. H. Santschi, R. Turnewitsch,
1022 J. T. Waples, and C. Xu (2012), Intercalibration studies of short-lived thorium-234 in the water
1023 column and marine particles, *Limnology and Oceanography: Methods*, 10(9), 631–644.
- 1024 Maiti, K., M. A. Charette, K. O. Buesseler, K. Zhou, P. Henderson, W. S. Moore, P. Morris, and
1025 L. Kipp (2015), Determination of particulate and dissolved ^{228}Th in seawater using a delayed
1026 coincidence counter, *Marine Chemistry*, 177, 196–202.
- 1027 Marchal, O., and P. J. Lam (2012), What can paired measurements of Th isotope activity and
1028 particle concentration tell us about particle cycling in the ocean?, *Geochimica et Cosmochimica*
1029 *Acta*, 90, 126–148.

1030 Marchal, O., R. François, and J. Scholten (2007), Contribution of ^{230}Th measurements to the esti-
1031 mation of the abyssal circulation, *Deep Sea Research Part I: Oceanographic Research Papers*,
1032 54(4), 557–585.

1033 Mawji, E., and et al. (2015), The GEOTRACES Intermediate Data Product 2014, *Marine Chem-*
1034 *istry*, 177, Part 1, 1–8.

1035 McCartney, M. S., S. L. Bennett, and M. E. Woodgate-Jones (1991), Eastward flow through the
1036 Mid-Atlantic Ridge at 11°N and its influence on the abyss of the eastern basin, *Journal of Phys-*
1037 *ical Oceanography*, 21(8), 1089–1121.

1038 McDonnell, A. M., and K. O. Buesseler (2010), Variability in the average sinking velocity of
1039 marine particles, *Limnology and Oceanography*, 55(5), 2085–2096.

1040 Mercier, H. (1986), Determining the general circulation of the ocean: a nonlinear inverse problem,
1041 *Journal of Geophysical Research: Oceans (19782012)*, 91(C4), 5103–5109.

1042 Mercier, H. (1989), A study of the time-averaged circulation in the western North Atlantic by
1043 simultaneous nonlinear inversion of hydrographic and current meter data, *Deep Sea Research*
1044 *Part A. Oceanographic Research Papers*, 36(2), 297–313.

1045 Mercier, H., M. Ollitrault, and P. Y. Le Traon (1993), A study of the time-averaged circulation
1046 in the western North Atlantic by simultaneous nonlinear inversion of hydrographic and current
1047 meter data, *Journal of physical oceanography*, 23(4), 689–715.

1048 Moran, S. B., M. A. Charette, J. A. Hoff, R. L. Edwards, and W. M. Landing (1997), Distribution
1049 of ^{230}Th in the Labrador Sea and its relation to ventilation, *Earth and Planetary Science Letters*,
1050 150(1), 151–160.

1051 Moran, S. B., C. C. Shen, H. N. Edmonds, S. E. Weinstein, J. N. Smith, and R. L. Edwards
1052 (2002), Dissolved and particulate ^{231}Pa and ^{230}Th in the Atlantic Ocean: constraints on interme-

1053 diate/deep water age, boundary scavenging, and $^{231}\text{Pa}/^{230}\text{Th}$ fractionation, *Earth and Planetary*
1054 *Science Letters*, 203(3), 999–1014.

1055 Murnane, R. J. (1994a), Determination of thorium and particulate matter cycling parameters at
1056 station P: A reanalysis and comparison of least squares techniques, *Journal of Geophysical*
1057 *Research: Oceans (1978 to 2012)*, 99(C2), 3393–3405.

1058 Murnane, R. J., J. L. Sarmiento, and M. P. Bacon (1990), Thorium isotopes, particle cycling mod-
1059 els, and inverse calculations of model rate constants, *Journal of Geophysical Research: Oceans*
1060 *(1978 to 2012)*, 95(C9), 16,195–16,206.

1061 Murnane, R. J., J. K. Cochran, and J. L. Sarmiento (1994b), Estimates of particle-and thorium-
1062 cycling rates in the northwest Atlantic Ocean, *Journal of Geophysical Research: Oceans (1978-*
1063 *2012)*, 99(C2), 3373–3392.

1064 Murnane, R. J., J. K. Cochran, K. O. Buesseler, and M. P. Bacon (1996), Least-squares estimates
1065 of thorium, particle, and nutrient cycling rate constants from the JGOFS North Atlantic Bloom
1066 Experiment, *Deep Sea Research Part I: Oceanographic Research Papers*, 43(2), 239–258.

1067 Nozaki, Y., and T. Nakanishi (1985), ^{231}Pa and ^{230}Th profiles in the open ocean water column,
1068 *Deep Sea Research Part A. Oceanographic Research Papers*, 32(10), 1209–1220.

1069 Nozaki, Y., Y. Horibe, and H. Tsubota (1981), The water column distributions of thorium isotopes
1070 in the western North Pacific., *Earth and Planetary Science Letters*, 54(2), 203–216.

1071 Nozaki, Y., H.-S. Yang, and M. Yamada (1987), Scavenging of thorium in the ocean, *Journal of*
1072 *Geophysical Research: Oceans (1978 to 2012)*, 92.C1(C1), 772–778.

1073 Ohnemus, D. C., and P. J. Lam (2015), Cycling of lithogenic marine Pprticulates in the US GEO-
1074 TRACES North Atlantic Zonal transect, *Deep Sea Research II*, 116, 283–302.

- 1075 Okubo, A., H. Obata, T. Gamo, and M. Yamada (2012), ^{230}Th and ^{232}Th distributions in mid-
1076 latitudes of the North Pacific Ocean: effect of bottom scavenging, *Earth and Planetary Science*
1077 *Letters*, 339, 139–150.
- 1078 Owens, S. A., K. O. Buesseler, and K. W. W. Sims (2011), Re-evaluating the ^{238}U -salinity rela-
1079 tionship in seawater: Implications for the ^{238}U ^{234}Th disequilibrium method, *Marine Chemistry*,
1080 126(1), 31–39.
- 1081 Owens, S. A., K. O. Buesseler, and S. Pike (2015), Thorium-234 as a tracer of particle dynamics
1082 and upper ocean export in the Atlantic Ocean, *Deep Sea Research-II*, 116, 42–59.
- 1083 Paillet, J., and H. Mercier (1997), An inverse model of the eastern North Atlantic general circu-
1084 lation and thermocline ventilation, *Deep Sea Research Part I: Oceanographic Research Papers*,
1085 44(8), 1293–1328.
- 1086 Polzin, K., K. Speer, J. Toole, and R. Schmitt (1996), Intense mixing of Antarctic Bottom Water in
1087 the equatorial Atlantic Ocean, *Nature*, 380, 54–57.
- 1088 Roy-Barman, M., L. Coppola, and M. Souhaut (2002), Thorium isotopes in the western Mediter-
1089 ranean Sea: an insight into the marine particle dynamics, *Earth and Planetary Science Letters*,
1090 196(3), 161–174.
- 1091 Rutgers van der Loeff, M., and G. W. Berger (1993), Scavenging of ^{230}Th and ^{231}Pa near the
1092 Antarctic polar front in the South Atlantic, *Deep Sea Research Part I: Oceanographic Research*
1093 *Papers*, 40(2), 339–357.
- 1094 Savoye, N., C. Benitez-Nelson, A. B. Burd, J. K. Cochran, M. Charette, K. O. Buesseler, G. A.
1095 Jackson, M. Roy-Barman, S. Schmidt, and M. Elsken (2006), ^{234}Th sorption and export models
1096 in the water column: A review, *Marine Chemistry*, 100, 234–249.
- 1097 Schmitz, W. J., and M. S. McCartney (1993), On the North Atlantic circulation, *Reviews of Geo-*
1098 *physics*, 31(1), 29–49.

- 1099 Scholten, J. C., M. Rutgers Van Der Loeff, and M. A (1995), Distribution of ^{230}Th and ^{231}Pa in the
1100 water column in relation to the ventilation of the deep Arctic basins, *Deep Sea Research Part II:*
1101 *Topical Studies in Oceanography*, 42(6), 1519–1531.
- 1102 Scholten, J. C., J. Fietzke, A. Mangini, C.-D. Garbe-Schönberg, A. Eisenhauer, R. Schneider,
1103 and P. Stoffers (2008), Advection and scavenging: Effects on ^{230}Th and ^{231}Pa distribution off
1104 Southwest Africa, *Earth and Planetary Science Letters*, 271, 159–169.
- 1105 Shen, C. C., C. C. Wu, H. Cheng, R. L. Edwards, Y. T. Hsieh, S. Gallet, C. C. Chang, T. Y. Li, D. D.
1106 Lam, A. Kano, M. Hori, and C. Spotl (2012), High-precision and high-resolution carbonate
1107 ^{230}Th dating by MC-ICP-MS with SEM protocols, *Geochimica et Cosmochimica Acta*, 99, 71–
1108 86.
- 1109 Stramma, L., H. Sabine, and J. Schafstall (2005), Water masses and currents in the upper tropical
1110 Northeast Atlantic off Northwest Africa, *Journal of Geophysical Research: Oceans (1978 to*
1111 *2012)*, 110(C12), 1–18.
- 1112 Tarantola, A., and B. Valette (1982), Generalized nonlinear inverse problems solved using the least
1113 squares criterion, *Reviews of Geophysics*, 20(2), 219–232.
- 1114 Turekian, K. K. (1977), The fate of metals in the ocean, *Geochimica et Cosmochimica Acta*, 41(8),
1115 1139–1144.
- 1116 Turner, J. T. (2002), Zooplankton fecal pellets, marine snow and sinking phytoplankton blooms,
1117 *Aquatic Microbial Ecology*, 27(1), 57–102.
- 1118 Vanmarcke, E. (1983), *Random Fields: Analysis and Synthesis*, MIT Press, Cambridge.
- 1119 Venchiarutti, C., C. Jeandel, and M. Roy-Barman (2008), Particle dynamics study in the wake of
1120 Kerguelen Island using thorium isotopes, *Deep Sea Research Part I: Oceanographic Research*
1121 *Papers*, 55(10), 1343–1363.

1122 Vogler, S., J. Scholten, M. Rutger van der Loeff, and A. Mangini (1998), ^{230}Th in the eastern North
1123 Atlantic: the importance of water mass ventilation in the balance of ^{230}Th , *Earth and Planetary*
1124 *Science Letters*, 156(1), 61–74.

1125 Wolberg, J. R. (1967), *Prediction Analysis.*, D. Van Nostrand, Princeton.

1126 Wunsch, C. (2006), *Discrete inverse and state estimation problems: with geophysical fluid appli-*
1127 *cations (Vol. 2)*, Cambridge University Press, Cambridge.

1128 Yu, E.-F., R. François, and M. P. Bacon (1996), Similar rates of modern and last-glacial ocean
1129 thermohaline circulation inferred from radiochemical data, *Nature*, 379, 689–694.

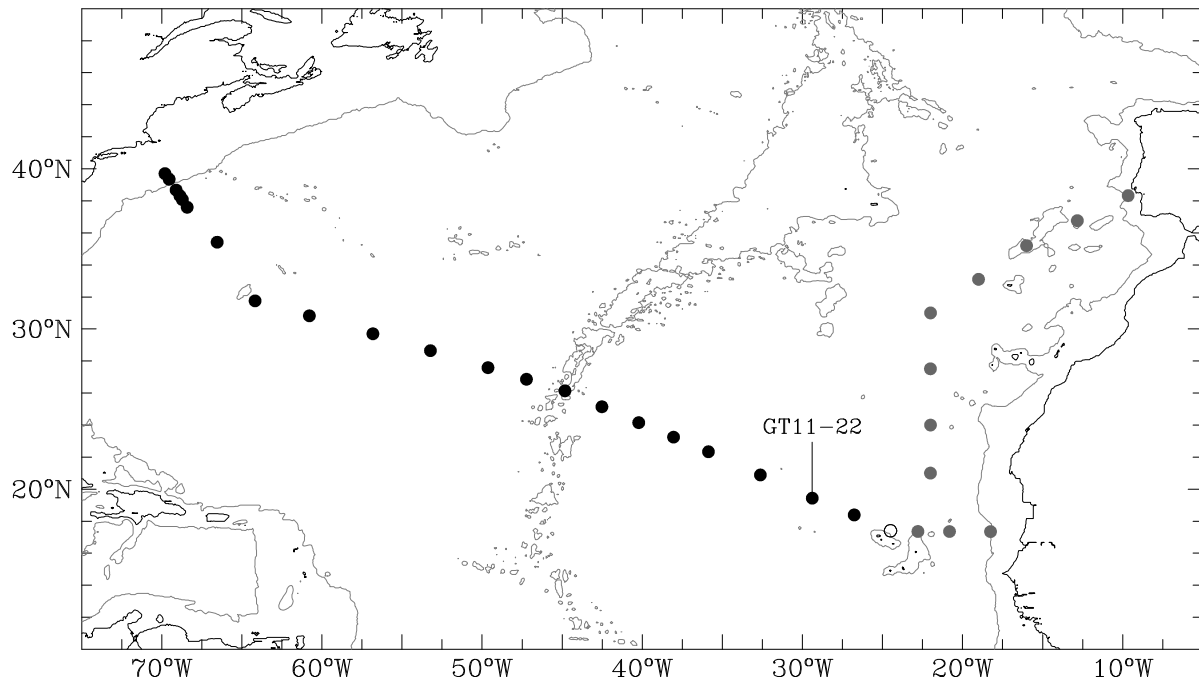


Figure 1: Stations occupied by the R/V Knorr during the GEOTRACES North Atlantic section. The latitude and longitude of the stations are from <http://data.bco-dmo.org/jg/dir/BCO/GEOTRACES/NorthAtlanticTransect/>. The grey dots show the stations occupied during the first leg (October 2010) and the black dots show the stations occupied during the second leg (November 2011). The open circle is both station 12 of the first leg and station 24 of the second leg. The data analyzed in this paper originate from station GT11-22, northwest of Cape Verde. The solid lines show the coastline (dark) and the 3000-m isobath (light) (bathymetric data are from <http://www.ngdc.noaa.gov/mgg/global>).

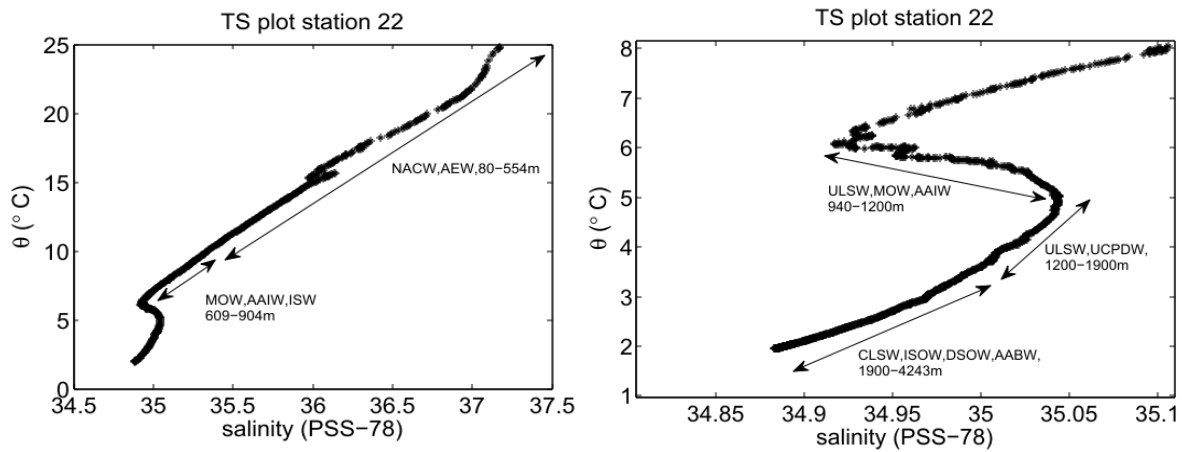


Figure 2: Plot of potential temperature vs. salinity for station GT11-22. Arrows indicate the estimated range of water masses. Shown are the labels and the depth range for the water masses. The left panel shows the $\theta - S$ plot from the surface to a depth of 904 m. The right panel shows the $\theta - S$ plot below 8°C. Data from [Jenkins et al. \(2015\)](#)

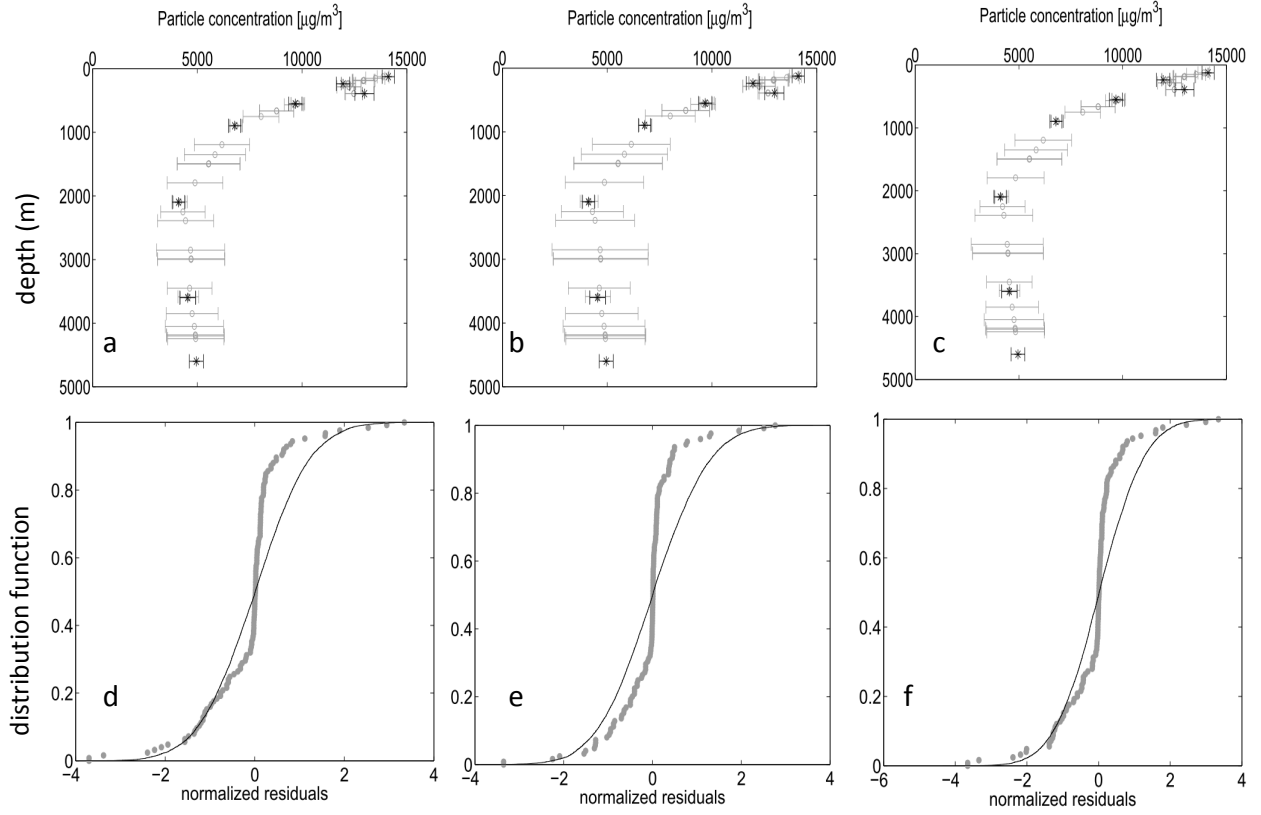


Figure 3: Top row (a-c): Measured (black asterisks) and interpolated (open circles) values of particle concentration (P) at station GT11-22 for three different field property variances: $\sigma_M^2 = 0.25\sigma_d^2$ (a), $\sigma_M^2 = 0.5\sigma_d^2$ (b), and $\sigma_M^2 = \sigma_d^2$ (c), where σ_d^2 is the variance of P measurements at station GT11-22. A length scale of $l_z = 1000$ m is used for each panel. Horizontal bars show ± 1 standard deviation. Measured particle concentrations are from [Lam et al. \(2015\)](#). The deepest measured value used in the interpolation of particle concentration is at 4600 m. Bottom row (d-f): Distribution function (DF) of the interpolation residuals normalized to measurement errors for all GT11-22 data used in this study. A normalized residual is defined as $(\hat{x}_i - x_{d,i})/\sigma_{d,i}$, where \hat{x}_i is the interpolated value at measurement depth level i , $x_{d,i}$ is the measured value at this level, and $\sigma_{d,i}$ is the error in the measurement at this level. For the three values of σ_M^2 , the difference $|\hat{x}_i - x_{d,i}|$ is less than $2\sigma_{d,i}$ for more than 95% of the data, which suggests an overfit (the solid line shows the normal DF).

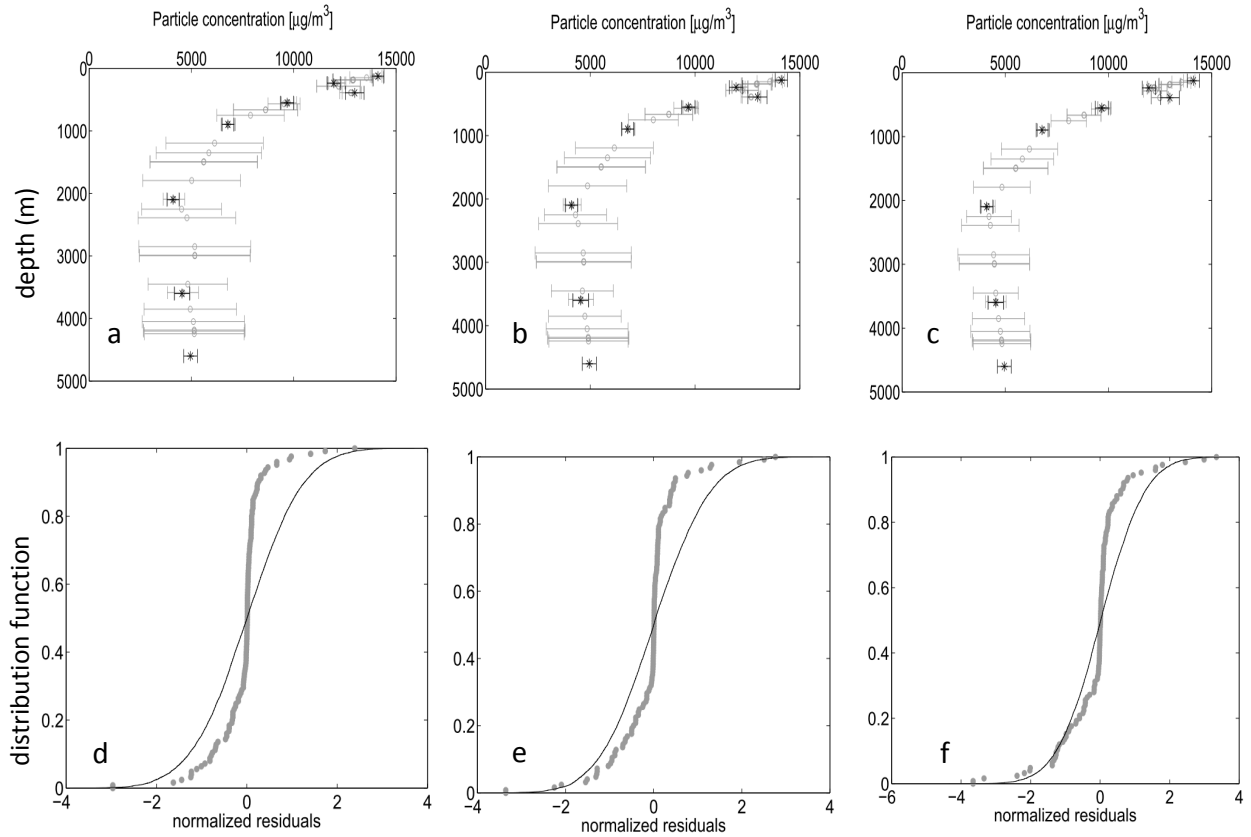


Figure 4: Same as Figure 1, but for three different vertical correlation scales: $l_z = 500$ m (a), $l_z = 1000$ m (b), and $l_z = 2000$ m (c). A field property variance of $\sigma_M^2 = 0.5\sigma_d^2$ is used for each panel. Measured particle concentrations are from [Lam et al. \(2015\)](#). Horizontal bars show ± 1 standard deviation.

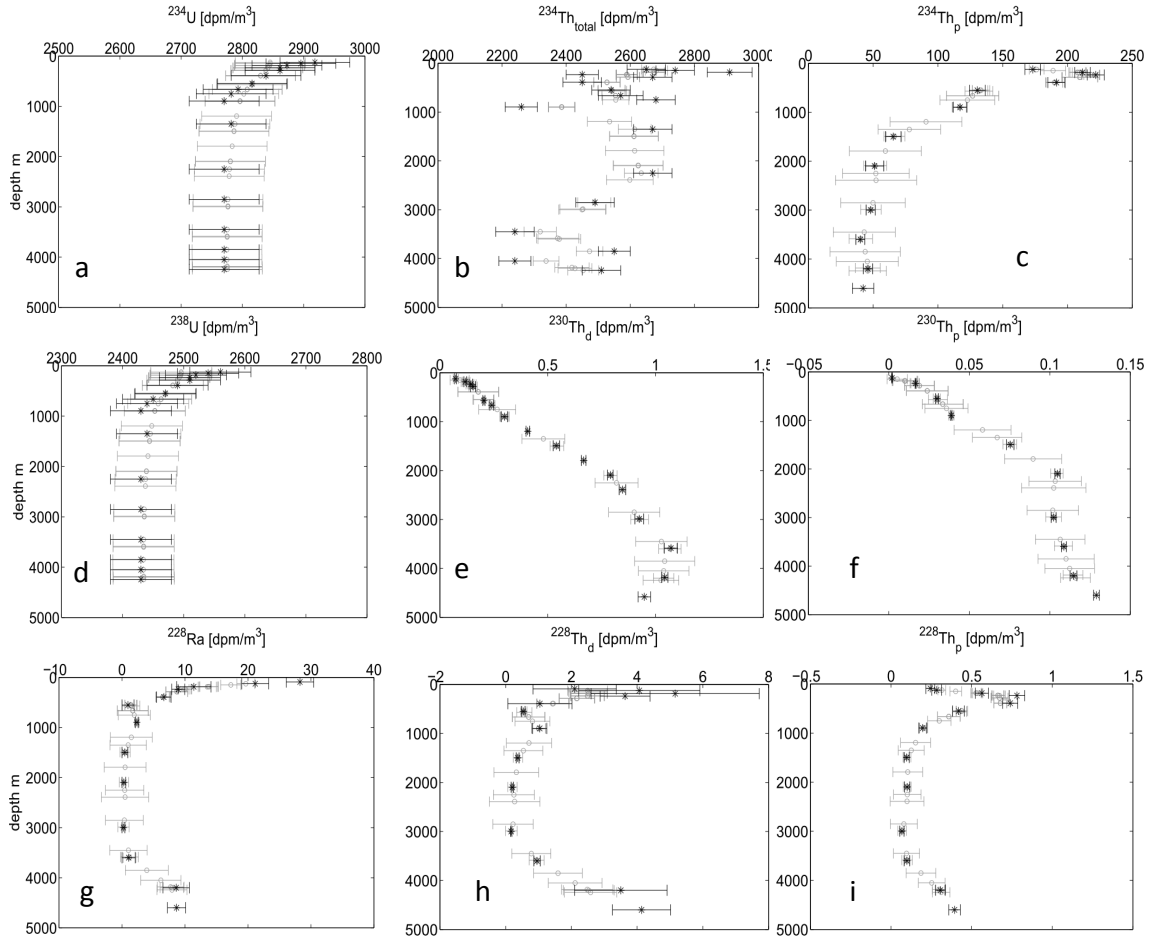


Figure 5: Profiles of Th isotope activities and their parent activities at station GT11-22. The black asterisks are the measured values. The open circles are the interpolated values obtained with $\sigma_M^2 = 0.5\sigma^2$, $l_z = 1000$ m.

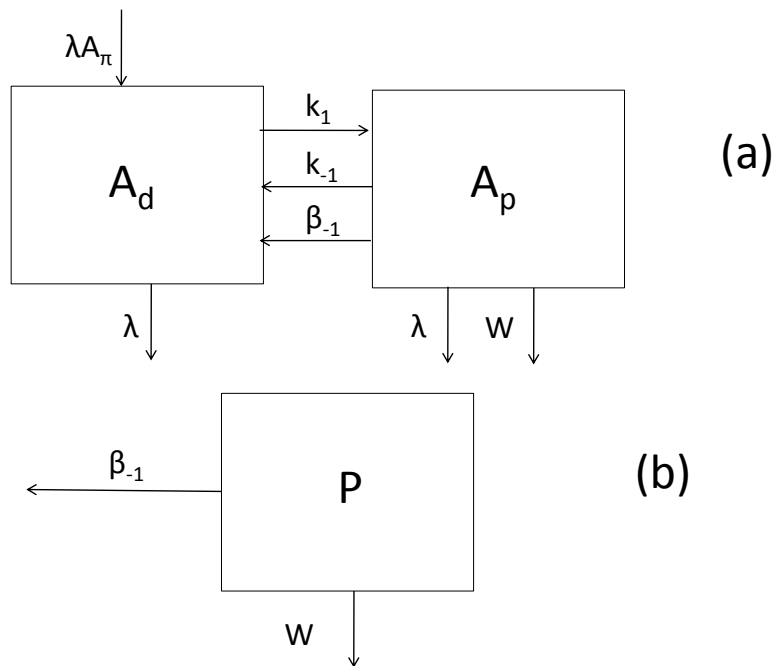


Figure 6: Schematic diagram of the single-particle class model of Th cycling (a) and particle cycling (b). 'A' and 'P' represent, respectively, the Th isotope activity and the particle concentration in the dissolved fraction ('d') or the particulate fraction ('p'). A_π is the activity of the parent isotope. The other symbols represent the rate parameters of solid-solution exchange (k_1 for adsorption, k_{-1} for desorption) and particle processes (β_{-1} for remineralization, and w for particle sinking). λ is the radioactive decay constant.

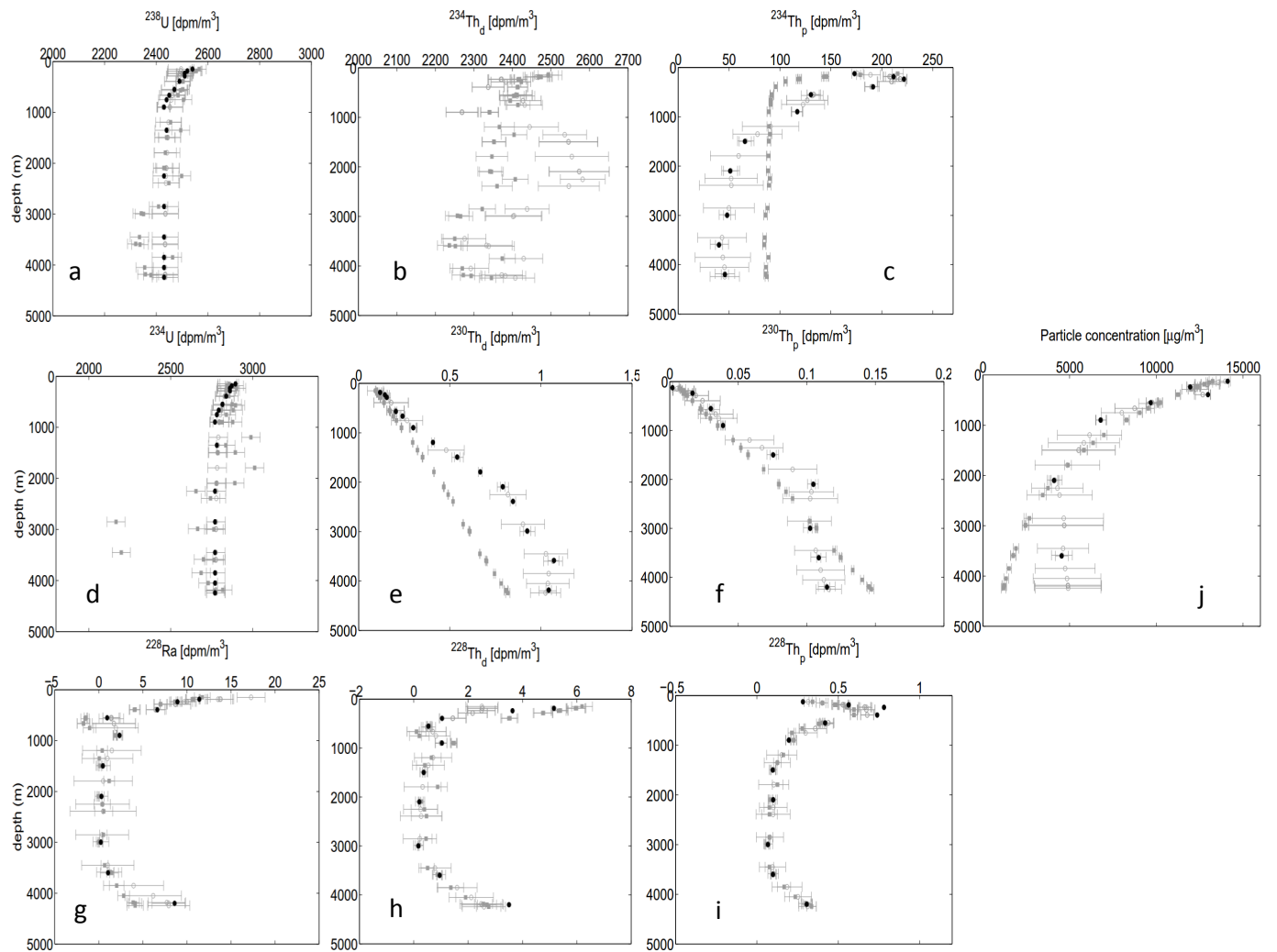


Figure 7: Radiochemical activities and particle concentrations at station GT11-22. The black circles are the measured values, the open circles are the interpolated values, and the grey squares are the fitted values for model V1.

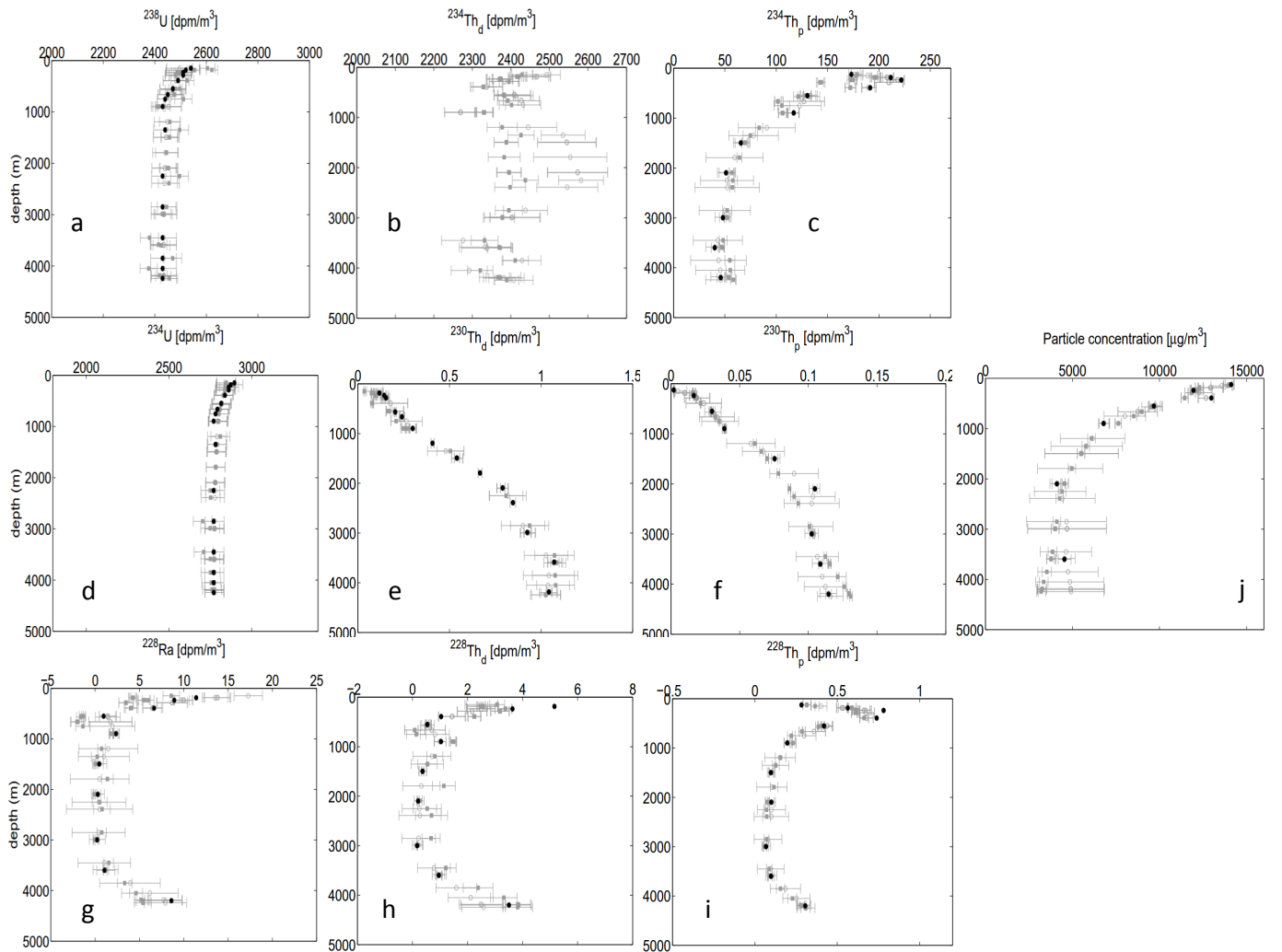


Figure 8: Same as figure 7, but for model V2.

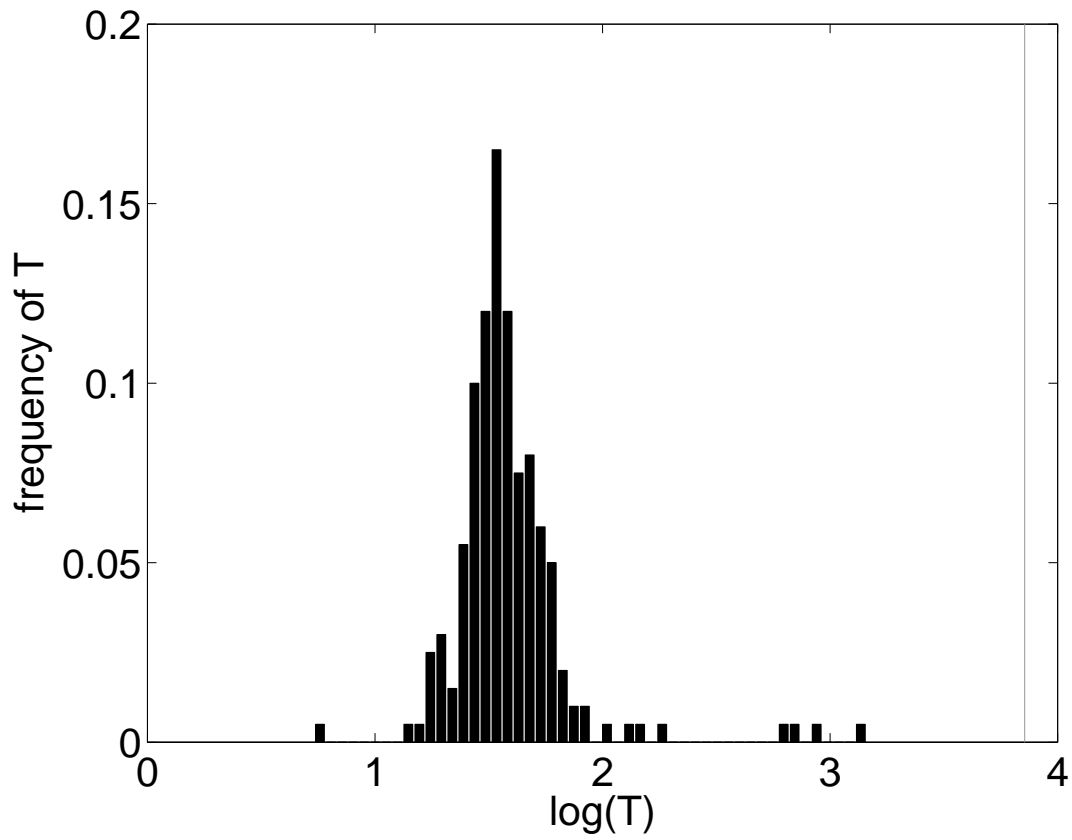


Figure 9: Histogram of the frequency of the test statistic T obtained from the bootstrap. The grey line shows the value of T obtained from our reference solution (section 3). The abscissa is the base-10 logarithm of the test statistic. Note that two negative values of T were found (-67 and -905), which are not shown in the figure

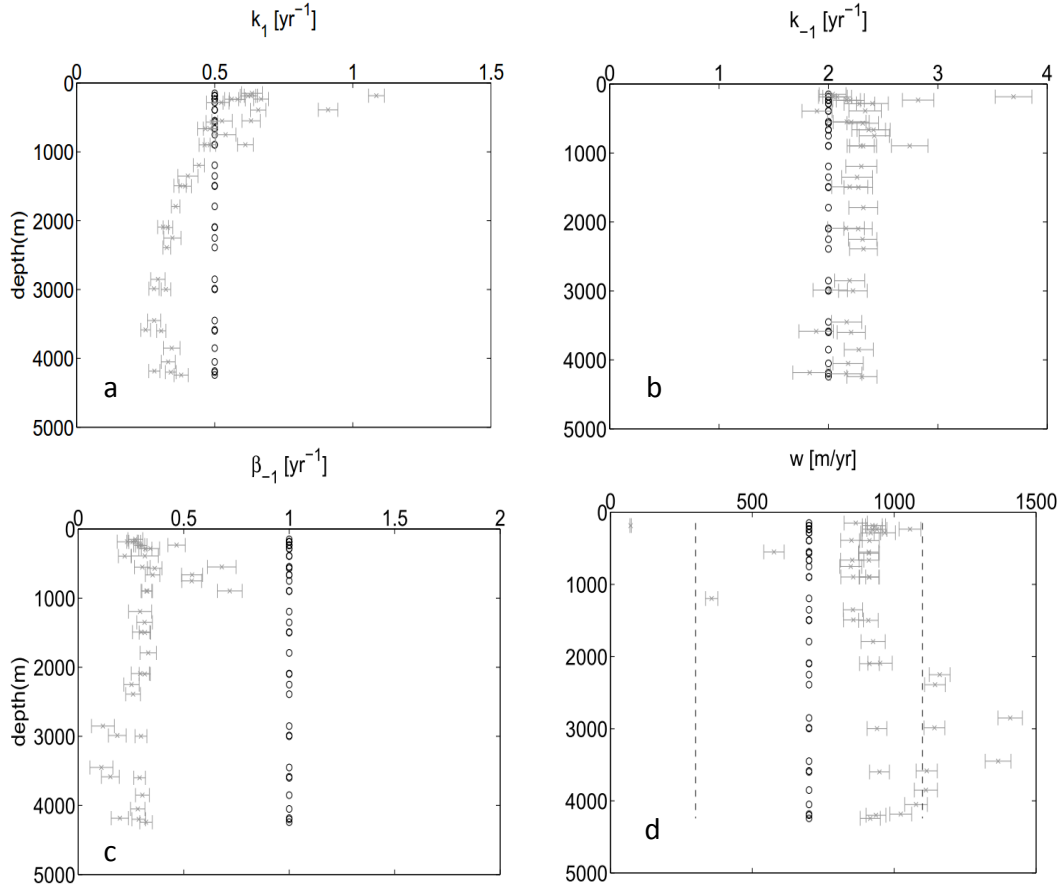


Figure 10: Rate parameters of Th and particle cycling at station GT11-22 as inferred from the combination of data with model V2. The open circles are the prior values ($k_1 = 0.5 \pm 5 \text{ yr}^{-1}$, $k_{-1} = 2 \pm 5 \text{ yr}^{-1}$, $\beta_1 = 1 \pm 10 \text{ yr}^{-1}$, $w = 700 \pm 400 \text{ m yr}^{-1}$). The vertical dashed lines in (d) show the range $[300-1100] \text{ m yr}^{-1}$ for the prior estimate of the particle sinking speed. The grey crosses are the posterior estimates ± 1 standard deviation (obtained by inversion). For comparison, the rate parameters inferred from the combination of data with model V1 are $k_1 = 0.49 \pm 0.01 \text{ yr}^{-1}$, $k_{-1} = 2.11 \pm 0.07 \text{ yr}^{-1}$, $\beta_1 = 0.46 \pm 0.02 \text{ yr}^{-1}$, $w = 725 \pm 7 \text{ m yr}^{-1}$

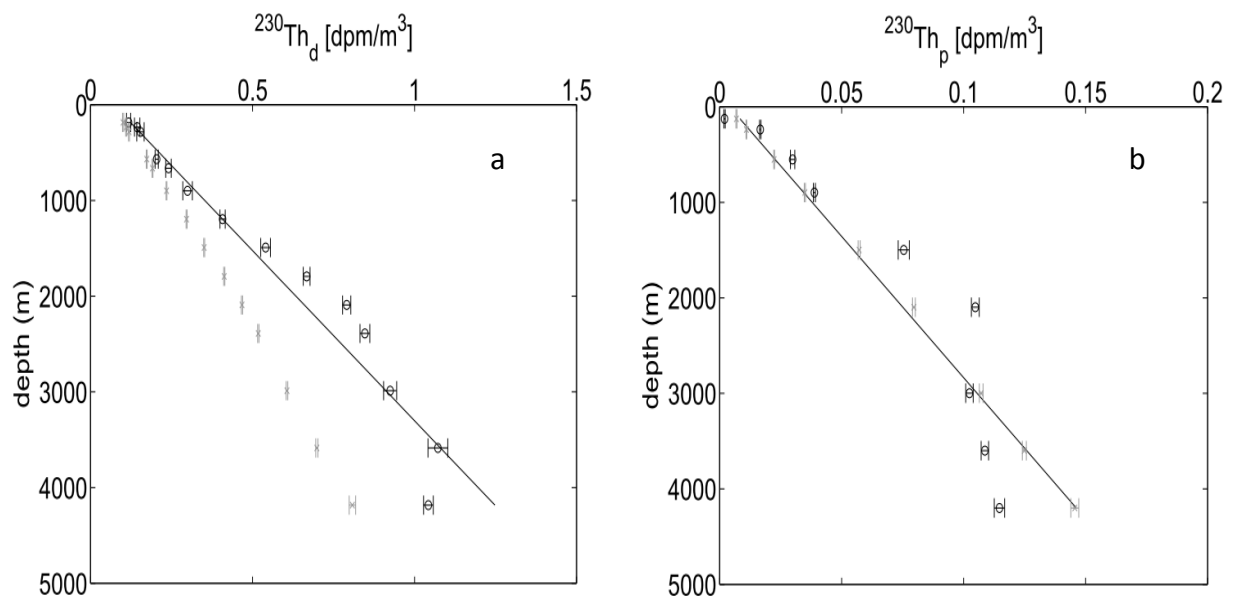


Figure 11: The left panel shows the $^{230}\text{Th}_d$ measurements at station GT11-22 (open circles), the posterior estimates of $^{230}\text{Th}_d$ from the fit of model V1 (grey crosses) to the entire data set ($^{234,238}\text{U}$, $^{228,230,234}\text{Th}_{d,p}$, P), and the line from fit of model V1 to only dissolved ^{230}Th data (derived from weighted least squares regression of $^{230}\text{Th}_d$ with depth). Horizontal bars are ± 1 standard deviation. The right panel is the same as the left panel, but for $^{230}\text{Th}_p$.

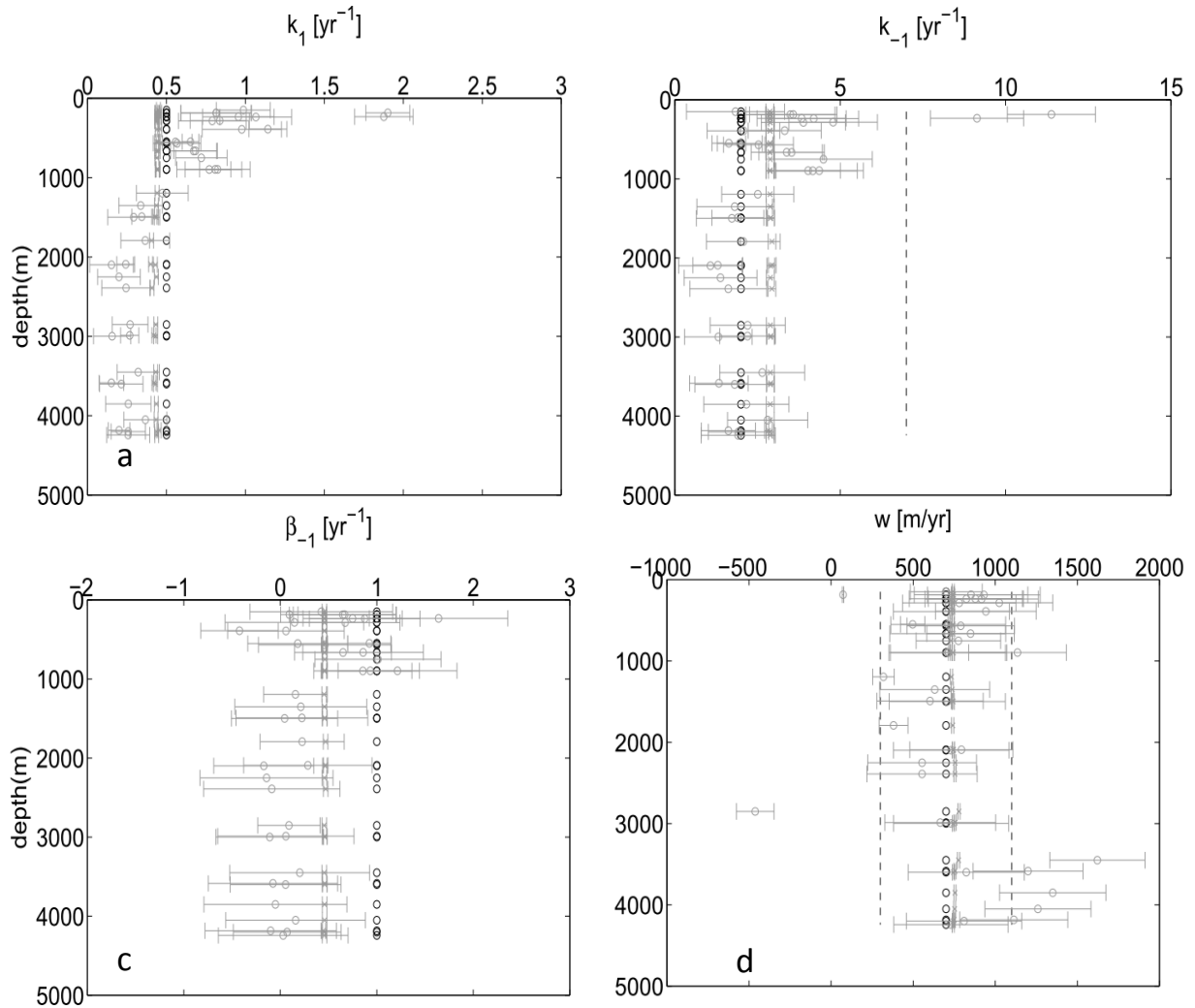


Figure 12: Rate parameters of Th and particle cycling at station GT11-22 as inferred from the combination of data with model V2. The open black circles are the prior estimates, and the posterior estimates for $\gamma = 0.01$ and $\gamma = 100$ are represented by open grey circles and grey crosses, respectively. Horizontal bars are ± 1 standard deviation. The vertical dashed lines show the range [value \pm one standard deviation] for the prior estimates.

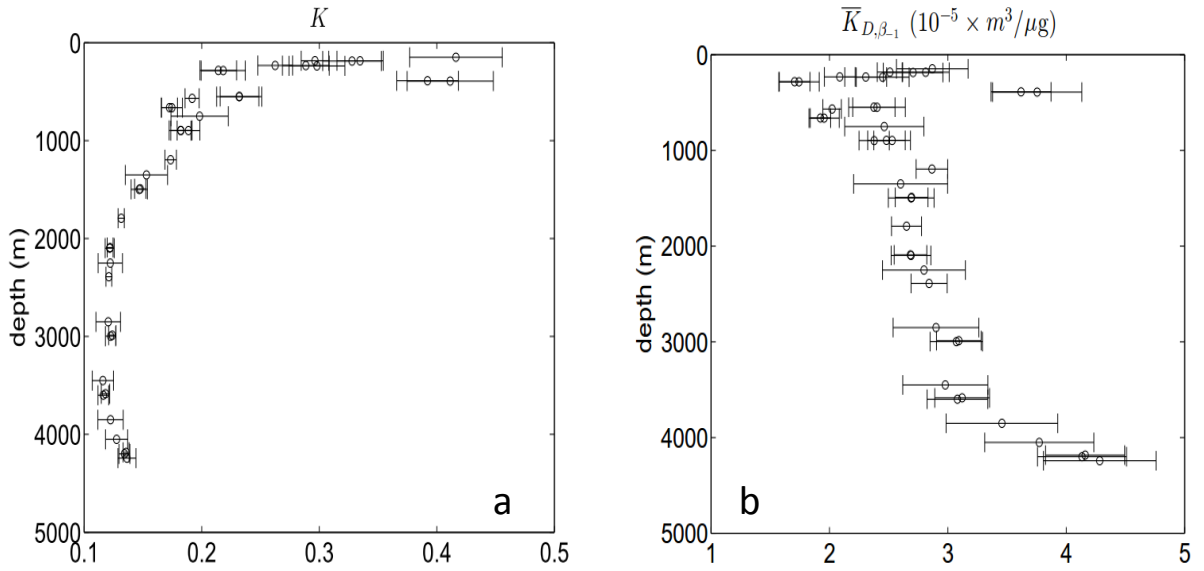


Figure 13: Profiles of $K = k_1/(k_{-1} + \beta_{-1})$ (a) and $\bar{K}_{D, \beta_{-1}} = K/P$ (b) at station GT11-22, as inferred from the combination of data with model V2. The horizontal bars show the errors (one standard deviation) derived from propagating the posterior errors of k_1 , k_{-1} , β_{-1} (and P for $\bar{K}_{D, \beta_{-1}}$), with due regard for the error covariances.

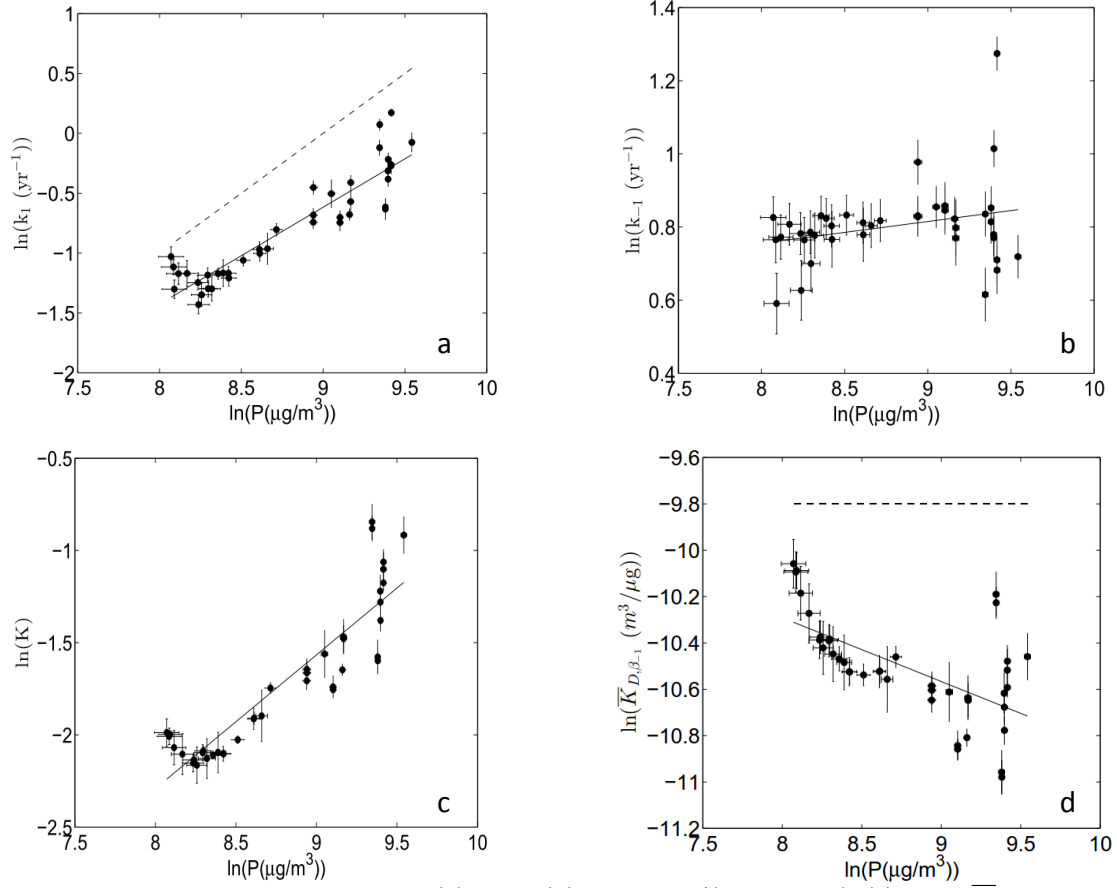


Figure 14: Variation of k_1 (a), k_{-1} (b), $K = k_1/(k_{-1} + \beta_{-1})$ (c), and $\overline{K}_{D,\beta_{-1}} = K/P$ (d) with particle concentration, as inferred from inversion of station GT11-22 data. Horizontal bars are ± 1 standard deviation. In each panel, the solid line is the ordinary least squares fit. The slopes of these lines are (a) 0.81 ± 0.06 , (b) 0.06 ± 0.03 (c) 0.73 ± 0.06 , and (d) -0.28 ± 0.06 . In panels a and d, the dashed line represents the slope expected in the absence of a particle concentration effect (the slope of this dashed line is 1 in panel a, and 0 in panel d).

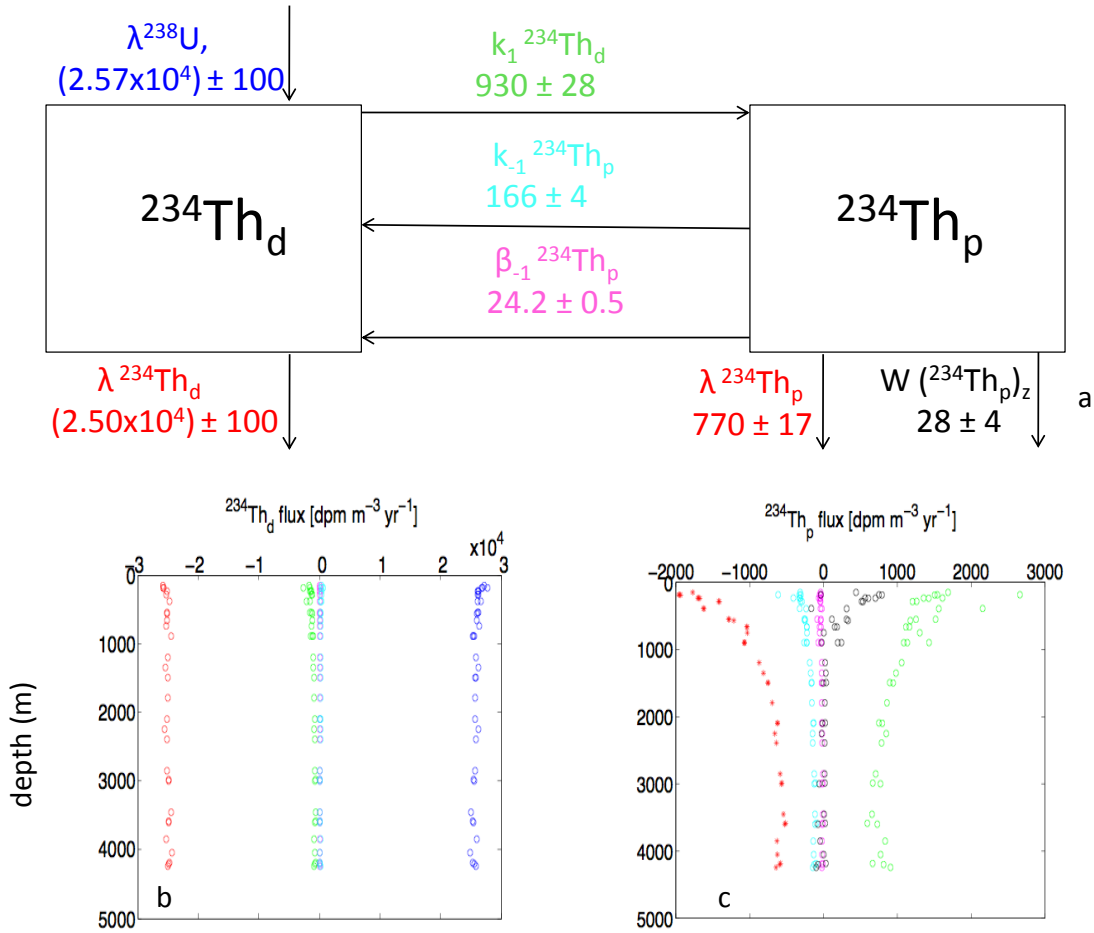


Figure 15: Panel (a) shows the ^{234}Th budget at station GT11-22. The displayed values are vertical averages (125-4243 m) in $\text{dpm m}^{-3} \text{yr}^{-1}$. Panel (b) and (c) show the vertical distribution of the ^{234}Th fluxes. In all panels, red for radioactive decay, blue for radioactive production, green for adsorption, cyan for desorption, magenta for remineralization, and black for the sinking flux.

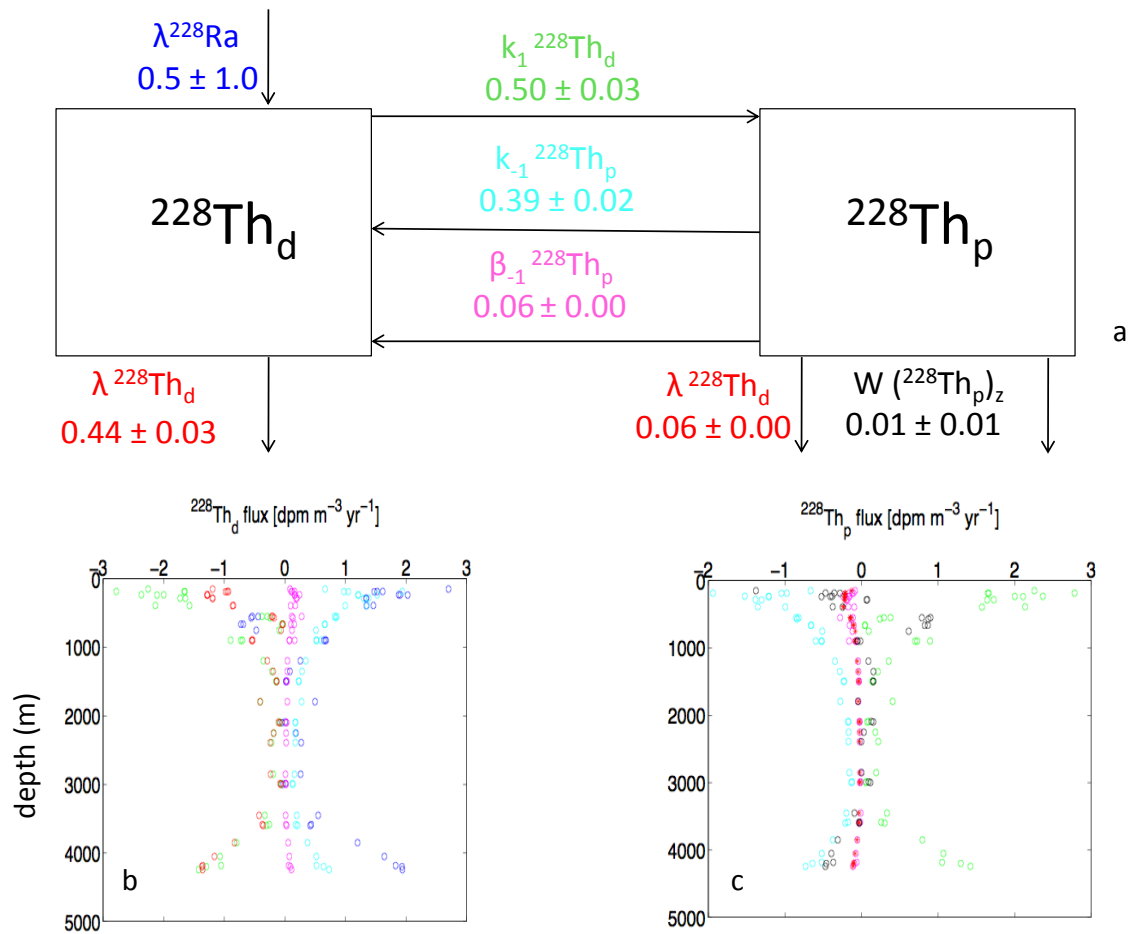


Figure 16: Same as Figure 13, but for ^{228}Th .

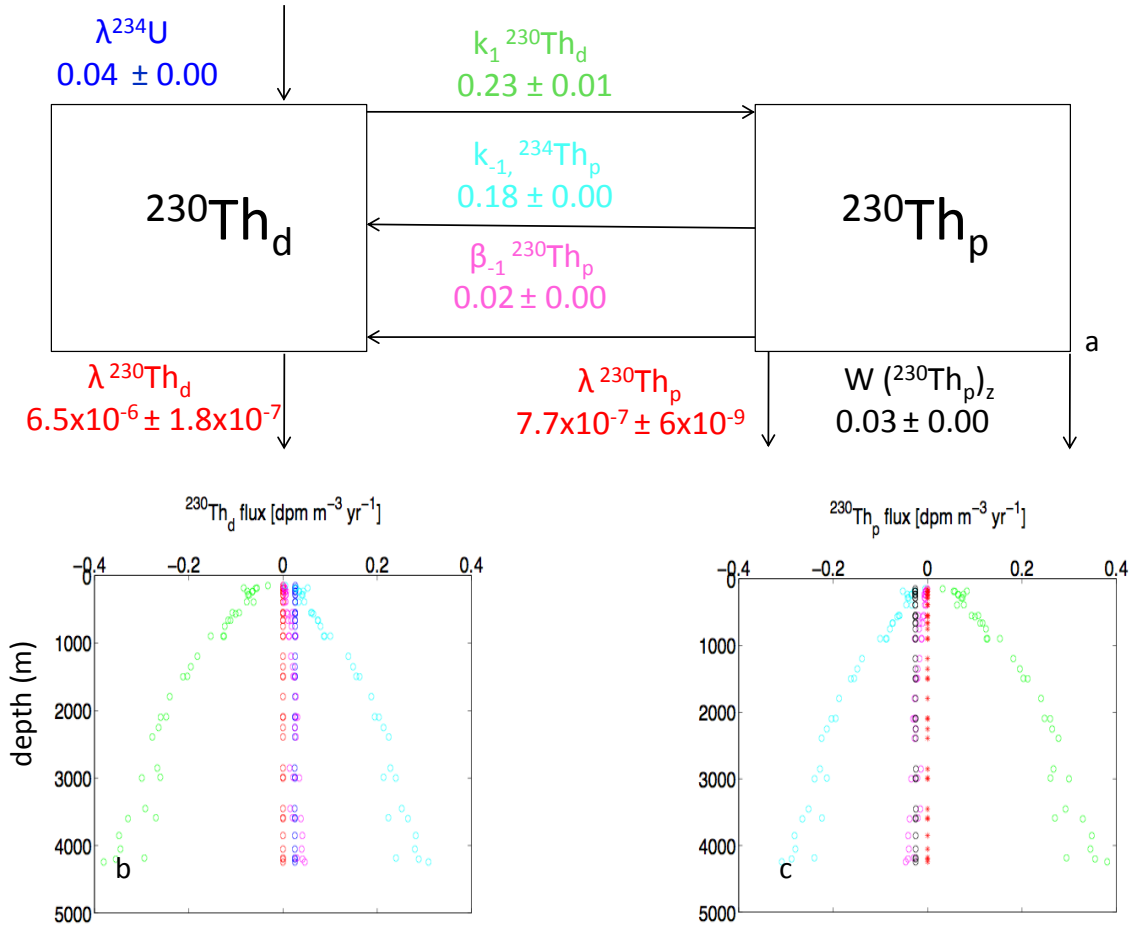


Figure 17: Same as Figure 13, but for ^{230}Th .

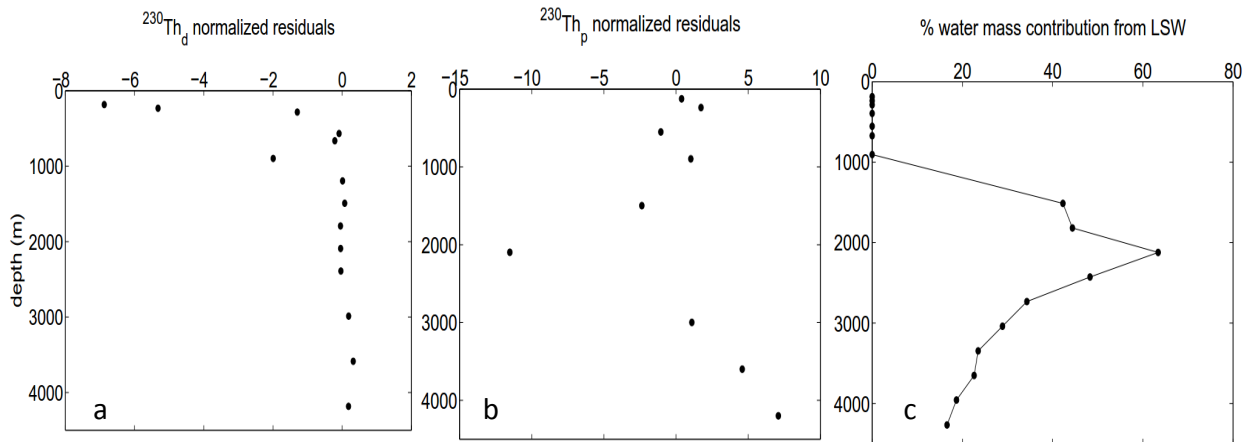


Figure 18: Panel (a) and (b) show the normalized residuals (eq. ??) of $^{230}\text{Th}_d$ and $^{230}\text{Th}_p$, respectively, for our reference solution (section 3). Panel (c) shows the sum of the proportions of Upper Labrador Sea Water and Central Labrador Sea Water at station GT11-22 (estimates from *Jenkins et al. (2015)*).

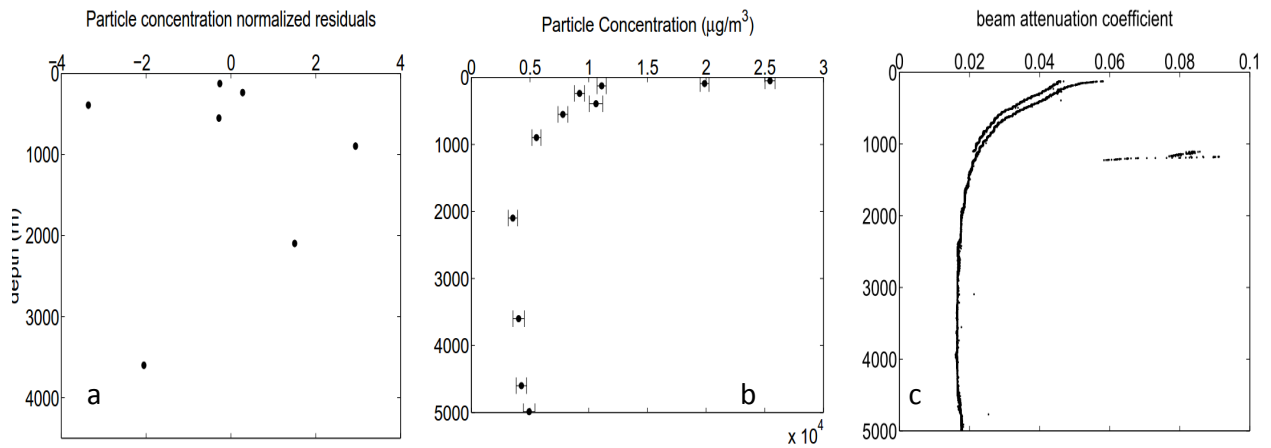


Figure 19: Panel (a) portrays the normalized residuals for particle concentration (eq. ??). Panel (b) portrays the particle concentrations ± 1 standard deviation from 125 m to 4989 m, the deepest depth at which small and large particles were sampled (data from [Lam et al. \(2015\)](#)). Panel (c) shows the beam attenuation coefficient measured using a WET Labs 25 cm pathlength C-Star transmissometer (660 nm) (data from [Anderson et al. \(2013\)](#)). The very large values between 1000 and 1500 m are real measurements.

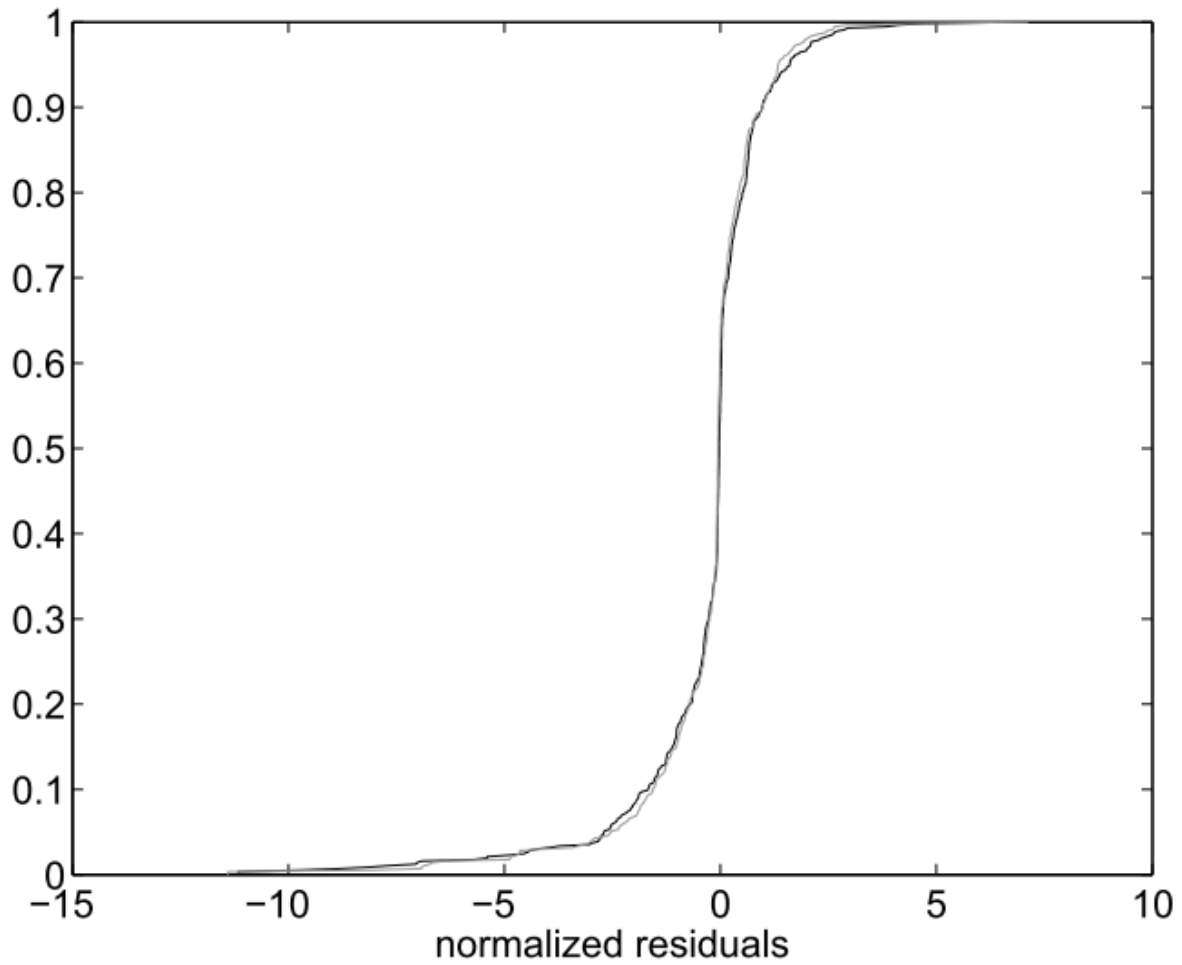


Figure 20: Normalized residuals of the fit of model V2 to station GT11-22 data for the reference case (Section 3) (black), and for the case where the prior $^{228,234}\text{Th}_p$ values are set to 20% less than their measured values (grey).

References

- Anderson, R. F., M. Q. Fleisher, and C. Hayes (2013), Transmissometer_GTC, *Biological and chemical oceanography data system*, BCO DMO, WHOI, http://data.bco-dmo.org/jg/info/BCO/GEOTRACES/NorthAtlanticTransect/Transmissometer_GTC%7Bdir=data.bco-dmo.org/jg/dir/BCO/GEOTRACES/NorthAtlanticTransect/,data=data.bco-dmo.org:80/jg/serv/BCO/GEOTRACES/NorthAtlanticTransect/GT10-11_trans_Cp_GTC.html0%7D?, accessed: 22 January, 2015.
- Jenkins, W. J., W. M. Smethie, and E. A. Boyle (2015), Water mass analysis for the U.S. GEOTRACES North Atlantic Sections, *Deep Sea Research Part II: Topical Studies in Oceanography*, 116, 6–20.
- Lam, P. J., D. C. Ohnemus, and M. E. Auro (2015), Size-fractionated major particle composition and concentrations from the U.S. GEOTRACES North Atlantic Zonal Transect, *Deep-Sea Research II*, 116, 303–320.